Protein-Metabolite Interactomics of Carbohydrate Metabolism Reveals Regulation of Lactate Dehydrogenase

One sentence short summary:

An interactomics platform identifies protein-metabolite interactions that adapt carbohydrate metabolism to a changing nutrient environment.

Authors:

Kevin G. Hicks[1], Ahmad A. Cluntun[1], Heidi L. Schubert[1], Sean R. Hackett[2], Jordan A. Berg[1], Paul G. Leonard[3,4], Mariana A. Ajalla Aleixo[5†], Youjia Zhou[6,7], Alex J. Bott[1], Sonia R. Salvatore[8], Fei Chang[8], Aubrie Blevins[1†], Paige Barta[1†], Samantha Tilley[1†], Aaron Leifer[1], Andrea Guzman[1], Ajak Arok[1], Sarah Fogarty[1,27], Jacob M. Winter[1], Hee-Chul Ahn[9‡], Karen N. Allen[10‡], Samuel Block[11‡], Iara A. Cardoso[5‡], Jianping Ding[12‡], Ingrid Dreveny[13‡], Clarke Gasper[14‡], Quinn Ho[14‡], Atsushi Matsuura[9‡], Michael J. Palladino[15‡], Sabin Prajapati[16,17‡], PengKai Sun[12‡], Kai Tittmann[16,17‡], Dean R. Tolan[14‡], Judith Unterlass[18‡], Andrew P. VanDemark[19‡], Matthew G. Vander Heiden[11,20‡], Bradley A. Webb[21‡], Cai-Hong Yun[22‡], PengKai Zhap[22‡], Bei Wang[6,7], Francisco J. Schopfer[8,23,24,25], Christopher P. Hill[1], Maria Cristina Nonato[5], Florian L. Muller[26], James E. Cox[1], Jared Rutter[1,27*]

Affiliations:

[1]Department of Biochemistry, University of Utah School of Medicine; Salt Lake City, USA.

[2]Calico Life Sciences LLC; South San Francisco, USA.

[3]Core for Biomolecular Structure and Function, University of Texas MD Anderson Cancer Center; Houston, USA.

[4]Institute for Applied Cancer Sciences, University of Texas MD Anderson Cancer Center; Houston, USA.

[5]Laboratório de Cristalografia de Proteinas, Faculdade de Ciências Farmacêuticas de Ribeirão Preto, Universidade de São Paulo; Ribeirão Preto, Brazil.

[6]School of Computing, University of Utah, Salt Lake City, USA.

[7]Scientific Computing and Imaging Institute, University of Utah, Salt Lake City, USA.

31 [8]Department of Pharmacology and Chemical Biology, University of Pittsburgh School of
32 Medicine. Pittsburgh, USA.
33 [9]Integrated Research Institute for Drug Development, College of Pharmacy, Dongguk University-
34 Seoul; Goyang, The Republic of Korea.
35 [10]Department of Chemistry, Boston University; Boston, USA.
36 [11]The Koch Institute for Integrative Cancer Research and Department of Biology, Massachusetts
37 Institute of Technology; Cambridge, USA.
38 [12]State Key Laboratory of Molecular Biology, Shanghai Institute of Biochemistry and Cell
39 Biology, Center for Excellence in Molecular Cell Science, University of Chinese Academy of
40 Sciences; Shanghai, China.
41 [13]Biodiscovery Institute, School of Pharmacy, University of Nottingham; Nottingham, UK.
42 [14]Department of Biology, Boston University; Boston, USA.
43 [15]Department of Pharmacology and Chemical Biology, University of Pittsburgh; Pittsburgh, USA.
44 [16]Department of Molecular Enzymology, Göttingen Center of Molecular Biosciences, University
45 of Göttingen; Göttingen, Germany.
46 [17]Department of Structural Dynamics, Max Planck Institute for Biophysical Chemistry; Göttingen,
47 Germany.
48 [18]Department of Oncology and Pathology, Karolinska Institute; Stockholm, Sweden.
49 [19]Department of Biological Sciences, University of Pittsburgh; Pittsburgh, USA.
50 [20]Dana-Farber Cancer Institute; Boston, USA
51 [21]Department of Biochemistry, West Virginia University; Morgantown, USA.
52 [22]Department of Biophysics, School of Basic Medical Sciences, Peking University Health Science
53 Center; Beijing, China.
54 [23]Pittsburgh Heart, Lung, Blood, and Vascular Medicine Institute, Pittsburgh, USA.
55 [24]Pittsburgh Liver Research Center, Pittsburgh, USA.
56 [25]Center for Metabolism and Mitochondrial Medicine, Pittsburgh, USA.
57 [26]Department of Cancer Systems Imaging, University of Texas MD Anderson Cancer Center;
58 Houston, USA.
59 [27]Howard Hughes Medical Institute, University of Utah School of Medicine; Salt Lake City, USA.
60 †Present addresses: Brazilian Nanotechnology National Laboratory, Brazilian Center for Research
61 in Energy and Materials; Campinas, Brazil (MAAA); Department of Molecular Biology, UT

62 Southwestern Medical Center; Dallas, USA (AB); Skaggs Graduate School of Chemical and
63 Biological Sciences, Scripps Research Institute; La Jolla, USA (PB); College of Medicine, Baylor
64 University; Houston, USA (ST).
65 ‡These authors are listed alphabetically.
66 *Corresponding author. Email: rutter@biochem.utah.edu

Abstract

Metabolic networks are interconnected and influence diverse cellular processes. The protein-metabolite interactions that mediate these networks are frequently low-affinity and challenging to systematically discover. We developed Mass spectrometry Integrated with equilibrium Dialysis for the discovery of Allostery Systematically (MIDAS) to identify such interactions. Analysis of 33 enzymes from human carbohydrate metabolism identified 830 protein-metabolite interactions including known regulators, substrates, and products, as well as previously unreported interactions. We functionally validated a subset of interactions, including the isoform-specific inhibition of lactate dehydrogenase by long-chain acyl-coenzyme A. Cells treated with fatty acids caused a loss of pyruvate-lactate interconversion dependent on lactate dehydrogenase isoform expression. These protein-metabolite interactions may contribute to the dynamic, tissue-specific metabolic flexibility that enables growth and survival in an ever-changing nutrient environment.

Main Text

Metabolites are the small molecule substrates, intermediates, and end products of metabolic pathways, and their interactions with proteins also communicate metabolic status to diverse cellular processes (Fig. 1A). Such regulatory interactions—both covalent and non-covalent—adapt cell behavior to dynamic nutrient availability and metabolic demand. The identification of protein-metabolite interactions (PMIs) has been sporadic and strategies to discover such interactions are limited. Some progress has been made (1, 2), but the nature of many PMIs complicates their identification. For example, to maximize dynamic regulatory potential, metabolites frequently interact with their target proteins with an affinity close to their cellular concentrations—often low micromolar to low millimolar. Therefore, we developed the highly sensitive Mass spectrometry Integrated with equilibrium Dialysis for the discovery of Allostery Systematically (MIDAS) platform to enable the systematic discovery of PMIs, including both low- and high-affinity interactions (3).

The MIDAS platform detects protein-metabolite interactions

MIDAS leverages the biophysical principle of equilibrium dialysis (Fig. 1B). Briefly, a purified protein is separated from a defined library of metabolites by a semi-permeable dialysis membrane that allows diffusion of metabolites, but not protein. After incubation, the system achieves relative equilibrium, such that the concentration of free (i.e., non-interacting) metabolites is similar in the protein- and metabolite-chambers (Fig. 1B-grey outlined symbols). However, the total concentration of those metabolites that interact with the protein is higher or lower in the protein-chamber relative to the metabolite-chamber dependent on binding affinity and mode of interaction (Fig. 1B-magenta triangles, yellow stars). The protein is then denatured and removed from the protein-chamber and the relative abundances of all metabolites from both chambers is quantified by high-throughput flow injection analysis mass spectrometry (FIA-MS). The fold change between the chambers is determined and then normalized and corrected to remove non-specific interactions (see Supplemental Methods section). A positive fold change indicates a direct PMI and is dependent on the binding affinity of the interaction. A negative fold change can result from the enzymatic conversion of the metabolite at a reaction rate faster than the diffusion rate across the membrane. PMIs that are not disrupted during protein

109 denaturation—both covalent and non-covalent—also produce negative fold changes as the
110 metabolite is removed with the protein.

111 The MIDAS metabolite library comprises 401 compounds that represent a sizable fraction
112 of the water-soluble, chemically-stable, FIA-MS-detectable, and commercially available
113 components of the human metabolome (Fig. S1A and Data S1). Due to the intrinsic differences in
114 chemical structure and ionization properties, not all metabolites could be analyzed with the same
115 FIA-MS parameters. We profiled each metabolite individually for its optimal FIA-MS ionization
116 and detection conditions (Data S2), and, guided by these criteria, divided the library into four pools
117 for multiplexed analysis (Fig. S1B and Data S1). We developed rapid FIA-MS methods, optimized
118 for each pool, that enabled quantification of the constituent metabolites.

119 We performed a pilot validation study using proteins with well-characterized metabolite
120 interactors. We analyzed three human proteins that regulate mechanistic target of rapamycin
121 complex 1 (mTORC1): cytosolic arginine sensor for mTORC1 subunit 1 (CASTOR1), which
122 binds arginine (4); Sestrin2, which binds leucine, isoleucine, and methionine (5); and Rheb, which
123 hydrolyzes guanosine triphosphate (GTP) to guanosine diphosphate (GDP) (6) (Fig. S1C). In each
124 case, the known metabolite-ligands of these proteins were the most enriched interactors detected
125 (Fig. 1C – E; see Table S1 for metabolite abbreviations). In addition to known interactions,
126 polyamine derivatives (1,3-diaminopropane, agmatine, and cadaverine) were found to bind
127 CASTOR1 and Sestrin2, suggesting potential feedback regulation given that the mTORC1
128 pathway promotes polyamine synthesis in some cancers (7). Thus, MIDAS effectively identified
129 known PMIs—regulators, substrates, and products.

130

131 **MIDAS reveals inter- and intrapathway interactions across carbohydrate metabolism**

132 The enzymes of carbohydrate metabolism drive the majority of cellular energy production
133 and biosynthetic precursor generation and are known to be regulated by metabolite interactions.
134 Therefore, we used MIDAS to profile 33 human enzymes spanning glycolysis, gluconeogenesis,
135 the tricarboxylic acid (TCA) cycle, and the serine biosynthetic pathway that branches from
136 glycolysis (Fig. S1C). In total, we identified 830 putative PMIs, many of which were previously
137 unknown (Data S4). Unsupervised hierarchical clustering (Fig. 2A – D) and multidimensional
138 scaling (Fig. 2E) of the PMI dataset demonstrated that structurally and functionally related proteins
139 frequently had similar metabolite interactions. For example, phosphoglycerate mutase (PGAM1

140 and PGAM2), enolase (ENO1 and ENO2), fructose bisphosphatase (FBP1 and FBP2), and lactate
141 dehydrogenase (LDHA and LDHB) all clustered closely with their isoform counterparts. However,
142 this was not observed across all enzyme isoforms and isozymes nor would it be expected given
143 that divergent evolution enables distinct metabolic function and regulation, particularly when
144 reflected in cell type-specific isoform expression. For example, pyruvate kinase muscle isoform 1
145 (PKM1) is primarily expressed in adult tissues whereas pyruvate kinase muscle isoform 2 (PKM2)
146 is expressed in fetal tissues and many cancer cells (8). The difference between PKM1- and PKM2-
147 metabolite interactomes may reflect their unique, context-dependent function and regulation.
148 Additionally, isocitrate dehydrogenase isozymes (IDH2 and IDH3), which catalyze similar
149 chemistry, but are evolutionarily and structurally unrelated (*9*), exhibited distinct metabolite
150 interactomes. We observed clustering of multiple nicotinamide adenine dinucleotide (NAD)-
151 dependent dehydrogenases: glyceraldehyde-3-phosphate dehydrogenase (GAPDH), LDHA,
152 LDHB, mitochondrial malate dehydrogenase (MDH2), and 3-phosphoglycerate dehydrogenase
153 (PHGDH), suggesting enzyme reaction class can drive the protein-metabolite interactome (Fig.
154 2E). An analogous clustering of structurally- and functionally-related metabolites was also
155 apparent, including nicotinamide-containing metabolites and flavin-adenine dinucleotide (Fig.
156 2B), phosphate-containing organic acids (Fig. 2C), and several nucleotide monophosphates (Fig.
157 2D).

158 Analysis of the 830 putative PMIs identified by the MIDAS platform showed that
159 carbohydrates exhibited the largest number of interactions with enzymes from carbohydrate
160 metabolism (Fig. 2F and S2). This likely reflects both substrate-product relationships as well as
161 the allosteric or orthosteric regulation of these enzymes by upstream or downstream metabolites
162 (i.e., feedforward and feedback regulation). The majority of non-carbohydrate PMIs involved
163 amino acids, nucleotides, and fatty acid derivatives. Such PMIs not only represent substrates and
164 products of enzymes in these pathways, but may reveal both intra- and inter-pathway regulation
165 of carbohydrate metabolism (Fig. 2G). Because MIDAS is an in vitro platform that lacks the
166 intracellular compartmentalization found in vivo, some of the putative PMIs are not predicted to
167 occur in intact cells (*10*); however, given the physiological plasticity of protein and metabolite
168 intracellular localization, such PMIs should not necessarily be ignored. We compared MIDAS data
169 to previously reported PMIs in the BRENDA and Recon3D databases (*11, 12*) using Fisher's exact
170 test and found that MIDAS significantly identified known substrates and products ($p < 2.0 \times 10^{-}$

171 [12]) and activators and inhibitors ($p < 4.7 \times 10^{-8}$). We propose that these MIDAS data provide a
172 detailed view of the integration of local and distal metabolic information in carbohydrate
173 metabolism.
174
175 **Structural analysis of metabolite interactions with enolase and fumarase**
176 We selected a subset of PMIs for deeper bioinformatic, biochemical, and structural
177 analysis. Enolase catalyzes the penultimate step in glycolysis, and the most enriched metabolite
178 for both isoforms (ENO1 and ENO2) was phosphoserine (pSer, Fig. 3A). pSer is the immediate
179 precursor for serine biosynthesis, which diverges from glycolysis upstream of enolase. Serine
180 allosterically activates PKM2 (*13*), the enzyme immediately downstream of enolase in glycolysis.
181 Differential scanning fluorimetry (DSF) (*14*), which measures the changing thermal stability of a
182 protein upon ligand binding, showed that pSer (but not serine, phosphotyrosine, or phosphate)
183 stabilized both ENO1 ($K_{D\,app}$ = 1.38 mM) and ENO2 ($K_{D\,app}$ = 1.15 mM) (Fig. 3B) with low affinity
184 similar to their substrate 2-phosphoglycerate (2PG) ($K_{D\,app}$ = 0.298 mM and 0.289 mM,
185 respectively). X-ray crystallography of the pSer-ENO2 complex showed that pSer was
186 asymmetrically bound to the ENO2 dimer at one of the two active sites and partially overlapped
187 with the 2PG phosphate binding site (Fig. 3C, D and S3A, B). Furthermore, pSer promoted an
188 "open" active site conformation relative to the substrate-bound complex, observed as repositioning
189 of loops 4 and 11 and alpha helices 7 and 11 (Fig. 3D). pSer only weakly inhibited in vitro enolase
190 activity (Fig. S3C). Thus, this binding event might modulate other enolase activities such as one
191 of its reported moonlighting functions (*15, 16*).
192 We identified 2-amino-3-phosphonopropionic acid (AP-3), a component of phosphonate
193 metabolism and the transamination product of 3-phosphonopyruvate (*17*), as a putative interactor
194 with fumarase, an enzyme in the TCA cycle that catalyzes the reversible hydration of fumarate to
195 malate (Fig. 3E). AP-3 induced the thermal stabilization of fumarase ($K_{D\,app}$ = 0.98 mM) similar
196 to its substrate, fumarate ($K_{D\,app}$ = 3.87 mM) (Fig. 3F). Kinetic assays demonstrated that AP-3
197 competitively inhibited fumarase (Fig. S3D), and, consistent with this, the crystal structure of the
198 complex revealed that AP-3 binds in the active site of fumarase similarly to the known inhibitor
199 citrate (Fig. 3G, H and S3E) (*18*). Although detected in human tissues and ubiquitous in microbial
200 metabolism (*19-21*), little is known about AP-3 metabolism in humans and the consequences of

201 fumarase modulation by AP-3. These findings demonstrate that without *a priori* information
202 MIDAS can identify previously unreported, low affinity, and functionally impactful PMIs.
203
204 **MIDAS identified known and previously unknown metabolite interactions**
205 MIDAS identified PMIs with previously known substrates, products, and regulators (Fig.
206 3I – N and S3F – L, stars). For example, glucose-6-phosphate isomerase (GPI) interacted with its
207 substrates, glucose-6-phosphate and fructose-6-phosphate (hexose-P) (Fig. 3I);
208 phosphofructokinase (PFKP) interacted with its product, fructose 1,6-bisphosphate
209 (F1,6BP/G1,6BP), and alternative substrate, sedoheptulose-7-phosphate (Sedo-7P) (*22*) (Fig. 3J);
210 GAPDH interacted with its substrate, NAD, and regulators, cyclic adenosine monophosphate
211 (cAMP), creatine-phosphate (P-creatine), and malonyl-CoA (*23-26*) (Fig. 3K); PKM2 interacted
212 with GDP and multiple amino acid regulators (*27*) (Fig. 3L); and PGAM1 and PGAM2 interacted
213 with their substrates 3-phosphoglycerate (3PG), 2,3-disphosphoglycerate (2,3-BPG), and
214 phosphoenolpyruvate (PEP) (Fig. 3N).
215 MIDAS also uncovered many previously unknown PMIs from diverse metabolic pathways
216 (Fig. 3I – N and S3F – L, circles). For example, acyl-coenzyme A, inositol phosphates,
217 nicotinamides, adenine nucleotides, and downstream glycolytic intermediates interacted with GPI
218 (Fig. 3I); inositol-1,4,5-triphosphate (Ins(1,4,5)P_3), 2,3-BPG, and 3-hydroxy-3-methylglutaryl
219 coenzyme A (HMG-CoA) intracted with GAPDH (Fig. 3K); PKM2 interacted with flavins, 5-
220 methyltetrahydrofolate (5-MTHF), and a thyroid hormone intermediate, 3,5-diiodo-L-tyrosine
221 (Fig. 3L). PKM2 is known to be allosterically regulated *in vitro* by thyroid hormone T_3 (*28*). Inter-
222 pathway metabolite interactions were also detected with the enzymes glucokinase (GCK), liver 6-
223 phosphofructokinase (PFKL), aldolase B (ALDOB), triosephosphate isomerase (TPI1),
224 phosphoglycerate kinase 1 (PGK1), phosphoserine aminotransferase 1 (PSAT1), and isocitrate
225 dehydrogenase 2 (IDH2) (Fig. S3F – L). Together these results suggest that MIDAS detects
226 extensive protein-metabolite interplay across the metabolic network.
227 MIDAS analysis of multiple isoforms of metabolic enzymes demonstrated both shared and
228 distinct metabolite interactions. Fructose bisphosphatase (FBP) catalyzes the conversion of
229 fructose-1,6-bisphosphate to fructose-6-phosphate. Both isoforms (FBP1 and FBP2) interacted
230 with various nucleotide monophosphates and 5-phospho-D-ribose 1-diphosphate (PRPP), the end
231 product of the pentose phosphate pathway and substrate for purine and pyrimidine metabolisms

232 (Fig. 3M). However, only FBP1 showed an interaction with glucosamine-6-phosphate, an often
233 rate-limiting intermediate in the hexosamine pathway, which is derived from fructose-6-
234 phosphate. These findings may reflect the expression differences between FBP1 (gluconeogenic
235 tissues) and FBP2 (non-gluconeogenic tissues) (https://www.gtexportal.org/home/). Similarly,
236 isoforms of phosphoglycerate mutase (PGAM1 and PGAM2) interacted with a large set of
237 metabolites, almost all of which were identical between them, except for Ins(1,4,5)P_3 with PGAM1
238 and phosphatidylinositol-4,5-bisphosphate C-6 (PIP2) and phosphatidylinositol-3,4,5-
239 triphosphate C-6 (PIP3) with PGAM2 (Fig. 3N). This might reflect differential membrane
240 recruitment and/or regulation of PGAM isoforms by phosphoinositide kinases, which are activated
241 by growth factor signaling (*29*). PMI differences between isoforms or isozymes may inform their
242 specific function and regulation.
243
244 **Lactate dehydrogenase A is inhibited by ATP**
245 Lactate dehydrogenase (LDH) catalyzes the reduction of pyruvate to lactate coincident
246 with the oxidation of NADH to NAD. Consumption of pyruvate, the end product of glycolysis, by
247 LDH competes with its mitochondrial uptake and oxidation by the TCA cycle to maximize ATP
248 production. When mitochondrial pyruvate oxidation is limited, such as in hypoxia or aerobic
249 glycolysis, LDH is required to regenerate NAD to enable continued glycolytic flux. The LDH
250 reaction is reversible and is required to use lactate, a major circulating carbohydrate in mammals
251 (*30*), as a fuel to support cellular functions. LDH is thus a key node in carbohydrate metabolism.
252 The two major isoforms, LDHA and LDHB, have distinct substrate reaction kinetics and
253 tissue expression (*31*). MIDAS analysis of LDHA and LDHB revealed interactions with several
254 metabolites, most of which were common to both proteins (Fig. 4A). These included the substrates
255 NADH and NAD and the structurally related nucleotides, nicotinamide mononucleotide and flavin
256 adenine dinucleotide, as well as the competitive inhibitor, oxaloacetate (*32*), and other keto-acids
257 related to the LDH substrates lactate and pyruvate (Fig. 4A, B). We also observed two other
258 classes of interacting metabolites, adenosine nucleotides and free and acylated coenzyme A. Using
259 DSF, we found that ATP interacted with LDHA and LDHB with a $K_{D\ app}$ = 0.636 mM and 0.697
260 mM, respectively (Fig. 4C), which is a low and biologically relevant affinity, given that the
261 intracellular steady state ATP concentration range is 1 to 8 mM (*33*). The observed interactions of
262 either LDH isoform with ADP and AMP may not be physiologically relevant given the disparity

263 between the $K_{D\ app}$ values and cellular concentrations of ADP and AMP (~0.4 mM and ~0.04 mM,
264 respectively (*34*)) (Fig. 4C). Enzymatic activity assays of the two LDH isoforms further supported
265 this conclusion as both AMP and ADP inhibited LDHA and LDHB only at supraphysiological
266 concentrations (Fig. 4D). Despite similar binding affinities to both LDHA and LDHB (Fig. 4C),
267 ATP inhibited only the LDHA isoform, with an IC_{50} of 2.3 mM and this inhibition appeared to be
268 competitive with NAD and lactate (Fig. 4D and S4A). This isoform-specific inhibition could relate
269 to the opposing effects of ATP binding on the thermal stability of the two proteins (Fig. 4C).
270
271 **LDHA, but not LDHB, is inhibited by fatty acyl-CoAs in vitro and in cells**
272 We investigated the putative interaction between the LDH isoforms and coenzyme A
273 (CoA) or CoA conjugated to short, medium, or long-chain fatty acids (i.e., acyl-CoAs).
274 Esterification of long-chain (>12 carbons) fatty acids to CoA is required for their intracellular
275 diffusion and transport into the mitochondrial matrix where they undergo β-oxidation to fuel ATP
276 production (*35*). The accumulation of these long-chain acyl-CoA species is a signal of carbon fuel
277 excess (*36*). We observed that acyl-CoAs inhibited LDHA as a function of fatty acid chain length.
278 Neither CoA alone nor any acyl-CoA with a fatty acid chain-length of up to eight carbons affected
279 enzyme activity, and C12:0-CoA (lauroyl-CoA) only inhibited LDHA with an IC_{50} >100 μM (Fig.
280 4E). However, long-chain acyl-CoAs such as C16:0-CoA (palmitoyl-CoA), C18:1-CoA (oleoyl-
281 CoA) and C20:0-CoA (arachidoyl-CoA) all inhibited LDHA with IC_{50} values of ~1 μM (Fig. 4E).
282 The inhibition of LDHA by palmitoyl-CoA was non-competitive with respect to both NAD and
283 lactate, suggesting that it likely binds to LDHA outside of the active site (Fig. S4B). Intriguingly,
284 LDHB, which shares 75% amino acid sequence identity with LDHA, was completely insensitive
285 to all tested acyl-CoAs, even at concentrations up to 100 μM (Fig. 4F).
286 Having observed that palmitoyl-CoA inhibited LDHA, but not LDHB, we used two
287 orthogonal approaches to test for a physical interaction. In a DSF assay, low micromolar
288 concentrations of palmitoyl-CoA (similar to the IC_{50}) induced the formation of a distinct thermo-
289 labile species of LDHA and a thermo-stable species of LDHB (Fig. S4C). LDHA and LDHB also
290 bound to palmitoyl-CoA immobilized on agarose beads and the binding of either protein was
291 disrupted by free palmitoyl-CoA, but not with buffer or C2:0-CoA (acetyl-CoA) (Fig. S4D). These
292 data indicate that LDHA and LDHB directly interact with palmitoyl-CoA with low micromolar
293 affinity.

294 Given that palmitoyl-CoA inhibited LDHA at physiological concentrations, we tested
295 whether this inhibition occurs in cells. We performed metabolic tracing experiments using H9c2
296 rat cardiomyoblasts, which were chosen because of their native expression of both isoforms,
297 wherein we deleted the *Ldha* or *Ldhb* gene, or both (Fig. S4E). We treated cells with ^{13}C-labeled
298 glucose in the presence or absence of BSA-conjugated palmitate, which allows for efficient
299 delivery of the fatty acid into the cell where it is esterified to palmitoyl-CoA (Fig. 4G). We used
300 mass spectrometry to measure the uptake and assimilation of ^{13}C into lactate. All four cell lines
301 (WT, *Ldha*$^{-/-}$, *Ldhb*$^{-/-}$, and *Ldha*$^{-/-}$ *Ldhb*$^{-/-}$) showed a similar (~80%) increase in intracellular
302 palmitate following incubation with its BSA-conjugate (Fig. S4F). Palmitate decreased the
303 labeling of lactate from ^{13}C-glucose in wild-type (WT) and *Ldhb*$^{-/-}$ cells, but not in cells lacking
304 LDHA (Fig. 4H and S4G, H), demonstrating that palmitate inhibition of glucose-to-lactate
305 conversion is dependent upon LDHA in these cells. Multiple enzymes in carbohydrate metabolism
306 are sensitive to acyl-CoA abundance (*37-41*), so, to more specifically interrogate the conversion
307 of lactate to pyruvate by LDH, we performed experiments wherein we followed the conversion of
308 ^{13}C-lactate to ^{13}C-pyruvate (Fig. 4I). Again, treatment with palmitate blunted the generation of
309 m+3 pyruvate in WT and *Ldhb*$^{-/-}$ cells, but pyruvate labeling in *Ldha*$^{-/-}$ or *Ldha*$^{-/-}$ *Ldhb*$^{-/-}$ cells
310 was unaffected (Fig. 4J, S4I-J).
311 To test the possibility that upstream or downstream intermediates in fatty acid metabolism
312 inhibit LDHA, we performed ^{13}C-glucose and ^{13}C-lactate tracing experiments in the presence of
313 triacsin C, an inhibitor of acyl-CoA synthase, which catalyzes fatty acid conjugation to coenzyme
314 A (Fig. S5A, C) (*42*). In both experiments, triacsin C prevented palmitate-mediated inhibition of
315 lactate and pyruvate labeling (Fig. S5B, D), thus demonstrating that conjugation to CoA is required
316 for palmitate to inhibit LDHA activity. To determine if catabolism of acyl-CoAs is required for
317 their inhibition of LDHA, we performed experiments using 2,2-dimethyl-palmitate (DiMePal) or
318 2,2-dimethyl-stearate (DiMeSte) (Fig. S6A). DiMePal and DiMeSte are dimethylated fatty acid
319 analogs that can be conjugated to CoA by acyl-CoA synthase, but cannot be further metabolized
320 via beta-oxidation (Fig. S6A, B). Similar to palmitoyl-CoA, DiMePal-CoA inhibited LDHA, but
321 not LDHB, in vitro (Fig. S6C, D). Tracing with either ^{13}C-glucose or ^{13}C-lactate was inhibited by
322 DiMePal or DiMeSte (Fig. S6E-I). These results suggest that the inhibition of LDHA by palmitate
323 is mediated by long-chain acyl-CoAs and not by upstream or downstream fatty acid intermediates.
324

325 **Discussion**

326 Both ATP and long-chain acyl-CoAs preferentially inhibited LDHA, but not LDHB.
327 LDHA and LDHB, the two dominant isoforms of lactate dehydrogenase, are expressed in a tissue-
328 specific pattern such that the liver almost exclusively expresses LDHA, whereas the heart has high
329 expression of LDHB (Fig. S7A, B). The IC_{50} for inhibition by ATP is well within the range of
330 normal intracellular ATP concentrations, so LDHA may be partially inhibited in all cells with
331 normal energy status. Given that the liver, the most LDHA-dominant tissue, catabolizes multiple
332 substrates, inhibition by ATP might be a mechanism to spare carbohydrates, like lactate, for other
333 tissues. The liver and heart have very different metabolic demands that mirror their LDHA and
334 LDHB expression differences, especially in the context of fatty acids. The heart is a "metabolic
335 omnivore" (*43*), acquiring energy from multiple nutrient sources. Expression of LDHB enables
336 carbohydrate metabolism, particularly lactate uptake and catabolism, even in the context of active
337 fatty acid metabolism (and potentially high acyl-CoA concentration). The liver plays a distinct and
338 critically important role in organismal metabolic homeostasis. LDHA inhibition by acyl-CoAs
339 could be a mechanism for the unexpected interplay of lactate, fatty acids, and gluconeogenesis
340 observed in animal studies (*44, 45*). Analysis of 928 cancer cell lines from DepMap (*46, 47*)
341 revealed a stronger negative correlation between lactate and long-chain acyl-carnitines
342 (intermediates in fatty acid metabolism) in the 70 cell lines that primarily express LDHA ($LDHA^{Hi}$
343 $LDHB^{Lo}$) relative to 858 cell lines that express both LDHA and LDHB ($LDHA^{Hi}$ $LDHB^{Hi}$) (Fig.
344 S7C-F). LDHA-specific inhibitors have been proposed to block aerobic glycolysis in cancers (*48,*
345 *49*), where perhaps the isoform-specific regulatory mechanism(s) of ATP and acyl-CoAs could be
346 exploited therapeutically.

347 This inter-pathway regulation between fatty acid and carbohydrate metabolisms is just one
348 potential example of the myriad metabolite-driven regulatory events that enforce organismal
349 homeostasis, which is vital to appropriately respond to stressors like the feed-fast cycle, exercise,
350 and infection. Interactions between proteins and metabolites may mediate much of this control.
351 We validated MIDAS as a platform for the discovery of these critical mechanisms, particularly for
352 the detection of low-affinity interactions. In complement to recent discoveries of functionally
353 important PMIs (*50-52*), MIDAS identified hundreds of putative interactions with the enzymes of
354 carbohydrate metabolism. Therefore, MIDAS serves as a conduit to identify, understand, and
355 exploit new modes of metabolic regulation across the protein-metabolite interactome.

356

357 **References**

358 1. M. Diether, U. Sauer, Towards detecting regulatory protein-metabolite interactions. *Curr*
359 *Opin Microbiol* **39**, 16-23 (2017).
360 2. M. Diether, Y. Nikolaev, F. H. Allain, U. Sauer, Systematic mapping of protein-metabolite
361 interactions in central metabolism of Escherichia coli. *Mol Syst Biol* **15**, e9008 (2019).
362 3. T. Orsak *et al.*, Revealing the allosterome: systematic identification of metabolite-protein
363 interactions. *Biochemistry* **51**, 225-232 (2012).
364 4. L. Chantranupong *et al.*, The CASTOR Proteins Are Arginine Sensors for the mTORC1
365 Pathway. *Cell* **165**, 153-164 (2016).
366 5. R. L. Wolfson *et al.*, Sestrin2 is a leucine sensor for the mTORC1 pathway. *Science* **351**,
367 43-48 (2016).
368 6. K. Inoki, Y. Li, T. Xu, K. L. Guan, Rheb GTPase is a direct target of TSC2 GAP activity
369 and regulates mTOR signaling. *Genes Dev* **17**, 1829-1834 (2003).
370 7. A. Zabala-Letona *et al.*, mTORC1-dependent AMD1 regulation sustains polyamine
371 metabolism in prostate cancer. *Nature* **547**, 109-113 (2017).
372 8. H. R. Christofk *et al.*, The M2 splice isoform of pyruvate kinase is important for cancer
373 metabolism and tumour growth. *Nature* **452**, 230-233 (2008).
374 9. P. Sun, Y. Liu, T. Ma, J. Ding, Structure and allosteric regulation of human NAD-
375 dependent isocitrate dehydrogenase. *Cell Discov* **6**, 94 (2020).
376 10. M. T. Alam *et al.*, The self-inhibitory nature of metabolic networks and its alleviation
377 through compartmentalization. *Nat Commun* **8**, 16018 (2017).
378 11. E. Brunk *et al.*, Recon3D enables a three-dimensional view of gene variation in human
379 metabolism. *Nat Biotechnol* **36**, 272-281 (2018).
380 12. A. Chang *et al.*, BRENDA, the ELIXIR core data resource in 2021: new developments and
381 updates. *Nucleic Acids Res* **49**, D498-D508 (2021).
382 13. B. Chaneton *et al.*, Serine is a natural ligand and allosteric activator of pyruvate kinase M2.
383 *Nature* **491**, 458-462 (2012).
384 14. F. H. Niesen, H. Berglund, M. Vedadi, The use of differential scanning fluorimetry to
385 detect ligand interactions that promote protein stability. *Nat Protoc* **2**, 2212-2221 (2007).

386 15. R. Lopez-Alemany *et al.*, Inhibition of cell surface mediated plasminogen activation by a
387 monoclonal antibody against alpha-Enolase. *Am J Hematol* **72**, 234-242 (2003).
388 16. S. Feo, D. Arcuri, E. Piddini, R. Passantino, A. Giallongo, ENO1 gene product binds to the
389 c-myc promoter and acts as a transcriptional repressor: relationship with Myc promoter-
390 binding protein 1 (MBP-1). *FEBS Lett* **473**, 47-52 (2000).
391 17. M. Kanehisa, S. Goto, KEGG: kyoto encyclopedia of genes and genomes. *Nucleic Acids*
392 *Res* **28**, 27-30 (2000).
393 18. T. Weaver, L. Banaszak, Crystallographic studies of the catalytic and a second site in
394 fumarase C from Escherichia coli. *Biochemistry* **35**, 13955-13965 (1996).
395 19. S. A. Tan, L. G. Tan, Distribution of ciliatine (2-aminoethylphosphonic acid) and
396 phosphonoalanine (2-amino-3-phosphonopropionic acid) in human tissues. *Clin Physiol*
397 *Biochem* **7**, 303-309 (1989).
398 20. R. H. Newman, K. R. Tate, Soil phosphorus characterisation by 31p nuclear magnetic
399 resonance. *Communications in Soil Science and Plant Analysis* **11**, 835-842 (1980).
400 21. L. L. Clark, E. D. Ingall, R. Benner, Marine phosphorus is selectively remineralized.
401 *Nature* **393**, 426-426 (1998).
402 22. K. Nakahigashi *et al.*, Systematic phenome analysis of Escherichia coli multiple-knockout
403 mutants reveals hidden reactions in central carbon metabolism. *Mol Syst Biol* **5**, 306 (2009).
404 23. S. Galvan-Pena *et al.*, Malonylation of GAPDH is an inflammatory signal in macrophages.
405 *Nat Commun* **10**, 338 (2019).
406 24. M. Nakano, S. Funayama, M. B. de Oliveira, S. L. Bruel, E. M. Gomes, D-glyceraldehyde-
407 3-phosphate dehydrogenase from HeLa cells--1. Purification and properties of the enzyme.
408 *Comp Biochem Physiol B* **102**, 873-877 (1992).
409 25. M. Oguchi, E. Gerth, B. Fitzgerald, J. H. Park, Regulation of glyceraldehyde 3-phosphate
410 dehydrogenase by phosphocreatine and adenosine triphosphate. IV. Factors affecting in
411 vivo control of enzymatic activity. *J Biol Chem* **248**, 5571-5576 (1973).
412 26. R. A. Kulkarni *et al.*, Discovering Targets of Non-enzymatic Acylation by Thioester
413 Reactivity Profiling. *Cell Chem Biol* **24**, 231-242 (2017).
414 27. M. Yuan *et al.*, An allostatic mechanism for M2 pyruvate kinase as an amino-acid sensor.
415 *Biochem J* **475**, 1821-1837 (2018).

416 28. K. Ashizawa, P. McPhie, K. H. Lin, S. Y. Cheng, An in vitro novel mechanism of
417 regulating the activity of pyruvate kinase M2 by thyroid hormone and fructose 1, 6-
418 bisphosphate. *Biochemistry* **30**, 7105-7111 (1991).
419 29. D. A. Fruman *et al.*, The PI3K Pathway in Human Disease. *Cell* **170**, 605-635 (2017).
420 30. S. Hui *et al.*, Glucose feeds the TCA cycle via circulating lactate. *Nature* **551**, 115-118
421 (2017).
422 31. A. Pesce, R. H. McKay, F. Stolzenbach, R. D. Cahn, N. O. Kaplan, The Comparative
423 Enzymology of Lactic Dehydrogenases. I. Properties of the Crystalline Beef and Chicken
424 Enzymes. *J Biol Chem* **239**, 1753-1761 (1964).
425 32. E. K. Wiese *et al.*, Enzymatic activation of pyruvate kinase increases cytosolic oxaloacetate
426 to inhibit the Warburg effect. *Nat Metab* **3**, 954-968 (2021).
427 33. T. W. Traut, Physiological concentrations of purines and pyrimidines. *Mol Cell Biochem*
428 **140**, 1-22 (1994).
429 34. G. J. Gowans, D. G. Hardie, AMPK: a cellular energy sensor primarily regulated by AMP.
430 *Biochem Soc Trans* **42**, 71-75 (2014).
431 35. S. M. Houten, S. Violante, F. V. Ventura, R. J. Wanders, The Biochemistry and Physiology
432 of Mitochondrial Fatty Acid beta-Oxidation and Its Genetic Disorders. *Annu Rev Physiol*
433 **78**, 23-44 (2016).
434 36. T. R. Koves *et al.*, Mitochondrial overload and incomplete fatty acid oxidation contribute
435 to skeletal muscle insulin resistance. *Cell Metab* **7**, 45-56 (2008).
436 37. Y. Zhang *et al.*, Long-chain fatty acyl-coenzyme A-induced inhibition of glucokinase in
437 pancreatic islets from rats depleted in long-chain polyunsaturated omega3 fatty acids. *Cell*
438 *Biochem Funct* **26**, 233-237 (2008).
439 38. A. L. Thompson, G. J. Cooney, Acyl-CoA inhibition of hexokinase in rat and human
440 skeletal muscle is a potential mechanism of lipid-induced insulin resistance. *Diabetes* **49**,
441 1761-1765 (2000).
442 39. C. M. Jenkins, J. Yang, H. F. Sims, R. W. Gross, Reversible high affinity inhibition of
443 phosphofructokinase-1 by acyl-CoA: a mechanism integrating glycolytic flux with lipid
444 metabolism. *J Biol Chem* **286**, 11937-11950 (2011).
445 40. A. L. Kerbey *et al.*, Regulation of pyruvate dehydrogenase in rat heart. Mechanism of
446 regulation of proportions of dephosphorylated and phosphorylated enzyme by oxidation of

447 fatty acids and ketone bodies and of effects of diabetes: role of coenzyme A, acetyl-
448 coenzyme A and reduced and oxidized nicotinamide-adenine dinucleotide. *Biochem J* **154**,
449 327-348 (1976).
450 41. Y. Nishida *et al.*, SIRT5 Regulates both Cytosolic and Mitochondrial Protein Malonylation
451 with Glycolysis as a Major Target. *Mol Cell* **59**, 321-332 (2015).
452 42. H. Tomoda, K. Igarashi, S. Omura, Inhibition of acyl-CoA synthetase by triacsins. *Biochim*
453 *Biophys Acta* **921**, 595-598 (1987).
454 43. H. Taegtmeyer, Carbohydrate interconversions and energy production. *Circulation* **72**,
455 IV1-8 (1985).
456 44. D. K. Sindelar, J. H. Balcom, C. A. Chu, D. W. Neal, A. D. Cherrington, A comparison of
457 the effects of selective increases in peripheral or portal insulin on hepatic glucose
458 production in the conscious dog. *Diabetes* **45**, 1594-1604 (1996).
459 45. D. K. Sindelar *et al.*, The role of fatty acids in mediating the effects of peripheral insulin
460 on hepatic glucose production in the conscious dog. *Diabetes* **46**, 187-196 (1997).
461 46. M. Ghandi *et al.*, Next-generation characterization of the Cancer Cell Line Encyclopedia.
462 *Nature* **569**, 503-508 (2019).
463 47. H. Li *et al.*, The landscape of cancer cell line metabolism. *Nat Med* **25**, 850-860 (2019).
464 48. J. Billiard *et al.*, Quinoline 3-sulfonamides inhibit lactate dehydrogenase A and reverse
465 aerobic glycolysis in cancer cells. *Cancer Metab* **1**, 19 (2013).
466 49. G. Rai *et al.*, Discovery and Optimization of Potent, Cell-Active Pyrazole-Based Inhibitors
467 of Lactate Dehydrogenase (LDH). *J Med Chem* **60**, 9184-9204 (2017).
468 50. G. A. Bezerra *et al.*, Crystal structure and interaction studies of human DHTKD1 provide
469 insight into a mitochondrial megacomplex in lysine catabolism. *IUCrJ* **7**, 693-706 (2020).
470 51. G. A. Bezerra *et al.*, Identification of small molecule allosteric modulators of 5,10-
471 methylenetetrahydrofolate reductase (MTHFR) by targeting its unique regulatory domain.
472 *Biochimie* **183**, 100-107 (2021).
473 52. Q. Hao *et al.*, Sugar phosphate activation of the stress sensor eIF2B. *Nature*
474 *communications* **12**, 3440 (2021).
475 53. J. Qin, G. Chai, J. M. Brewer, L. L. Lovelace, L. Lebioda, Structures of asymmetric
476 complexes of human neuron specific enolase with resolved substrate and product and an

477 analogous complex with two inhibitors indicate subunit interaction and inhibitor
478 cooperativity. *J Inorg Biochem* **111**, 187-194 (2012).
479

Acknowledgements

We thank members of the Rutter lab for helpful discussions and comments on the manuscript. We thank Daniel E. Gottschling (Calico Life Sciences, LLC) for helpful discussions throughout the project. We thank Roche and Navitor for providing proteins for MIDAS analyses. We thank director Crystal Davey of the University of Utah Mutation Generation and Detection Core for providing CRISPR reagents, cell genotyping services, and construction of bacterial expression vectors. We thank the director Bai Luo of the University of Utah Drug Discovery Core Facility for generating mutant cell lines. Metabolomics analysis was performed in the Metabolomics Core Facility at the University of Utah. Mass spectrometry equipment was obtained through NCRR Shared Instrumentation Grant 1S10OD016232-01, 1S10OD018210-01A1 and 1S10OD021505-01. The support and resources from the Center for High Performance Computing at the University of Utah are gratefully acknowledged. JR is an investigator of the Howard Hughes Medical Institute.

Funding

National Institutes of Health grant T32DK091317 (KGH)

National Institutes of Health grant T32DK007115 (KGH)

National Institutes of Health grant U54DK110858 (JR)

National Institutes of Health grant R35GM131854 (JR)

National Institutes of Health grant R01DK108859 (DRT)

National Institutes of Health grant R01GM103369 (APV)

National Institutes of Health grant R35CA242379 (MGVH)

National Institutes of Health grant R01CA201276 (MGVH)

National Institutes of Health grant T32-GM007287 (SB)

National Institutes of Health grant U54DK110858 (JEC)

National Institutes of Health grant R01HD04346 (MJP)

National Institutes of Health grant R01HD105311 (MJP)

National Institutes of Health grant R01 GM125944 (FJS)

National Institutes of Health grant R01 DK112854 (FJS)

National Institutes of Health grant F99CA253744 (JAB)

National Institutes of Health grant 5K00CA212445 (AJB)

National Institutes of Health grant T32DK091317 (AL)

National Institutes of Health grant F30CA243440 (JMW)

National Science Foundation DBI-1661375 (BW)

National Science Foundation: IIS-1513616 (BW)

National Research Foundation of Korea grant 2021R1F1A1063558 (HCA)

National Natural Science Foundation of China grant 32071207 (CHY)

German Research Foundation SFB860 (KT)

Conselho Nacional de Desenvolvimento Científico e Tecnológico 308769/2019-8 (MCN)

Fundação de Amparo à Pesquisa do Estado de São Paulo 2008/08262-6 (MCN)

Coordenação de Aperfeiçoamento de Pessoal de Nível Superior 88882.328384/2010-01 (MAAA)

Conselho Nacional de Desenvolvimento Científico e Tecnológico 154690/2018-0 (MAAA)

Calico LLC (JR)

Nora Eccles Treadwell Foundation (JR, CPH)

Howard Hughes Medical Institute (JR)

Howard Hughes Faculty Scholars grant (MGVH)

The Emerald Foundation (MGVH)

The Lustgarten Foundation (MGVH)

527 The Ludwig Center at MIT (MGVH)

528 The MIT Center for Precision Cancer Medicine (MGVH)

529 University of Nottingham (ID)

530 University of West Virginia (BAW)

531

532 **Author Contributions**

533 Conceptualization: KGH, JR

534 Methodology: KGH, JEC

535 Software: JAB, SRH, YZ, BW

536 Validation: KGH, AAC, PL, MAAA, AJB, AMB, PB, ST, AL, AG, AA, SRS, FJS

537 Formal analysis: KGH, JAB, SRH, AJB

538 Investigation: KGH, AAC, PGL, MAAA, AJB, AMB, PB, ST, SRS, AL, AG, AA, JMW

539 Resources: HLS, MAAA, HA, KNA, SB, IAC, JD, ID, CG, QH, AM, MJP, SP, PS, KT, DRT, JU,

540 APV, MGVH, BAW, CY, PZ, CPH, MCN FLM, Navitor, Roche, JEC, FC, FJS

541 Writing - Original Draft: JR, KGH

542 Writing - Review & Editing: JR, KGH, SF, AAC, PGL, MAAA, ST, JMW, IAC, MGV, MCN,

543 JEC, FJS

544 Visualization: KGH, AAC, JAB, YZ, AJB, JMW, AMB, PB, ST, AL, AG, AA, SRS, FJS, BW

545 Supervision: JR, KGH

546 Project administration: JR, KGH

547 Funding acquisition: JR, KGH

548

549 **Competing Interests**

KGH and JR are inventors of MIDAS technology that has been licensed to Atavistik Bio, for which KGH is a consultant and JR is a founder. FC and FJS have financial interest in Furanica Inc. FJS has financial interest in Creegh Pharma Inc. SRH is an employee of Calico Life Sciences. All other authors declare that they have no competing interests.

Data and Materials Availability

All data are available in the main text, supplementary materials, or online, as indicated. Protein expression plasmids generated for this study are available from Addgene (accessions pending). The MIDAS R analysis tool is available at https://github.com/KevinGHicks/MIDAS. The *Electrum* vizualization tool is available at https://github.com/Electrum-app/Electrum/releases/tag/v0.0.0. The coordinates for atomic models have been deposited in the Protein Data Bank under accession codes 7MBH (pSer-ENO2) and 7LUB (AP-3-FH). MIDAS FIA-MS spectra for proteins analyzed in this study are available at https://www.metabolomicsworkbench.org/ (accessions pending).

Supplementary Materials

Materials and Methods

Figs. S1 to S7

Tables S1, S2, and S3

Data S1 to S4

Fig. 1

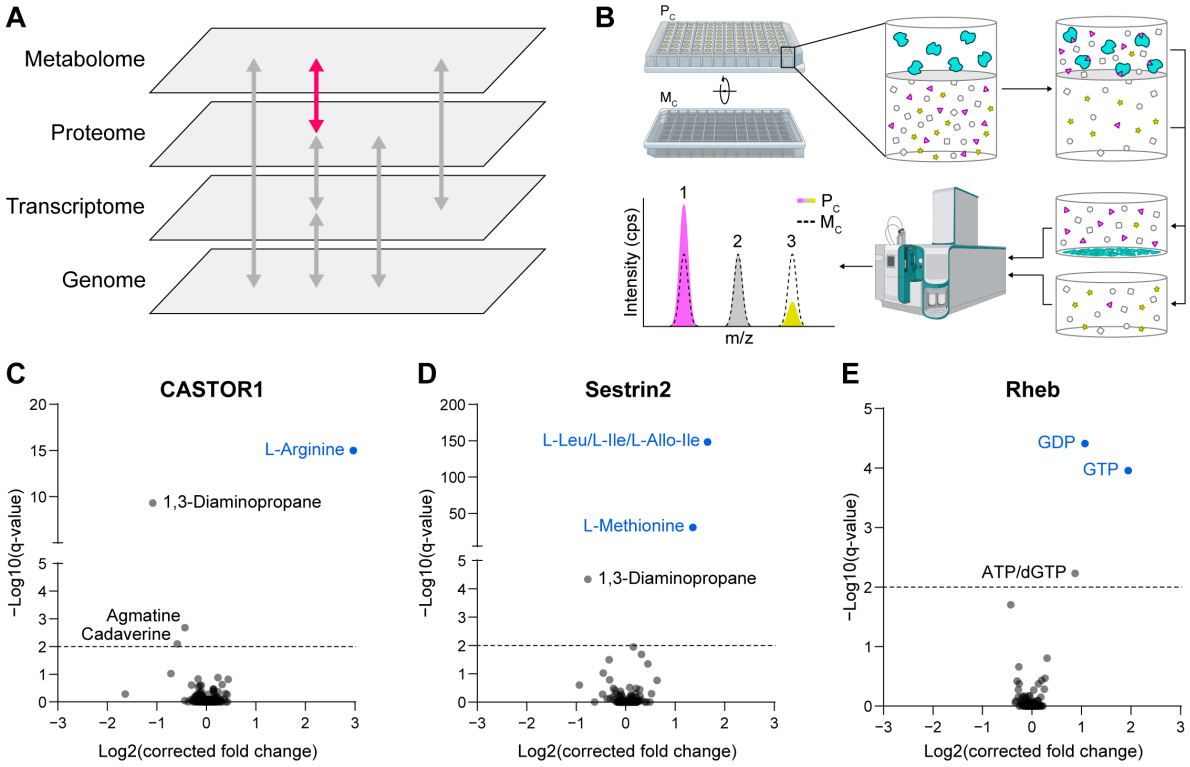
A
Metabolome
Proteome
Transcriptome
Genome
B
Pc
Mc
Intensity (cps)
m/z
1
2
3
C
CASTOR1
L-Arginine
1,3-Diaminopropane
Agmatine
Cadaverine
−Log10(q-value)
Log2(corrected fold change)
D
Sestrin2
L-Leu/L-Ile/L-Allo-Ile
L-Methionine
1,3-Diaminopropane
E
Rheb
GDP
GTP
ATP/dGTP

570 **Figure 1. MIDAS is a platform for the systematic discovery of protein-metabolite**
571 **interactions.**
572 **(A)** Biological systems are organized into domains of information (labeled grey panes). Flow of
573 information within and between these domains is transmitted through direct interactions and
574 underlies biological function (arrows). The MIDAS platform provides protein-metabolite
575 interaction (PMI) discovery (pink arrow). **(B)** The MIDAS platform is an equilibrium dialysis
576 tandem flow injection analysis mass spectrometry (FIA-MS) approach. (Top, left and center)
577 Purified proteins (cyan) are loaded into the protein-chamber (P_c) and defined pools of metabolites
578 into the metabolite-chamber (M_c), separated by a protein-impermeable dialysis membrane. (Top,
579 right) The system is incubated to relative equilibrium. (Bottom, right and center) Proteins are
580 removed by precipitation, metabolites in the P_c and M_c are sampled, and the relative abundance of
581 metabolites from both chambers are quantified using FIA-MS. (Bottom, left) PMIs are observed
582 as an increase (1) or decrease (3) in metabolite abundance in the P_c relative to the M_c (dotted peak).
583 Metabolites that have equal abundance in the P_c relative to the M_c (2) are defined as non-interacting
584 with the target protein. **(C, D, E)** Volcano plots of MIDAS analyses of the mTORC1 regulators
585 CASTOR1, Sestrin2, and Rheb. Significant PMIs are labeled; previously known interactions are
586 blue. All proteins were screened by triplicate equilibrium dialysis and technical triplicate FIA-MS
587 injections. Significant PMIs identified by MIDAS are labeled and have a q-value < 0.01 (dotted
588 line).

Fig. 2

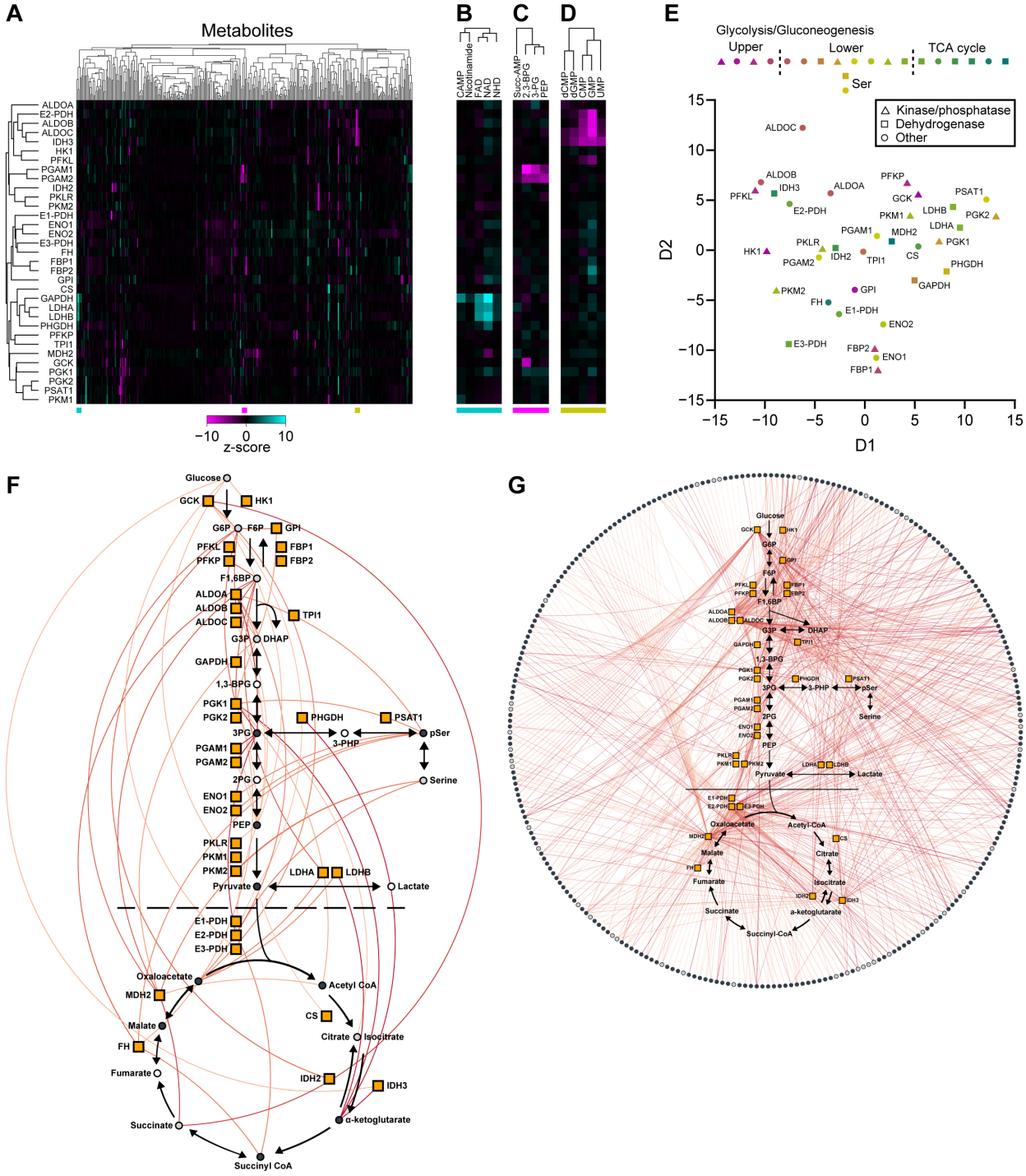
A
Metabolites
ALDOA
E2-PDH
ALDOB
ALDOC
IDH3
HK1
PFKL
PGAM1
PGAM2
IDH2
PKLR
PKM2
E1-PDH
ENO1
ENO2
E3-PDH
FH
FBP1
FBP2
GPI
CS
GAPDH
LDHA
LDHB
PHGDH
PFKP
TPI1
MDH2
GCK
PGK1
PGK2
PSAT1
PKM1
−10 0 10
z-score
B
CAMP
Nicotinamide
FAD
NAD
NHD
C
Succ-AMP
2,3-BPG
3-PG
PEP
D
dCMP
dGMP
CMP
GMP
UMP
E
Glycolysis/Gluconeogenesis
Upper
Lower
TCA cycle
Ser
Kinase/phosphatase
Dehydrogenase
Other
D1
D2
F
Glucose
GCK
HK1
G6P
F6P
GPI
PFKL
PFKP
FBP1
FBP2
F1,6BP
ALDOA
ALDOB
ALDOC
TPI1
G3P
DHAP
GAPDH
1,3-BPG
PGK1
PGK2
PHGDH
PSAT1
3PG
3-PHP
pSer
PGAM1
PGAM2
Serine
2PG
ENO1
ENO2
PEP
PKLR
PKM1
PKM2
LDHA
LDHB
Pyruvate
Lactate
E1-PDH
E2-PDH
E3-PDH
Oxaloacetate
Acetyl CoA
MDH2
CS
Malate
Citrate
Isocitrate
FH
Fumarate
IDH2
IDH3
Succinate
α-ketoglutarate
Succinyl CoA
G

590 **Figure 2. The protein-metabolite interactome of human carbohydrate metabolism.**
591 **(A)** Heatmap representation of MIDAS PMIs of 33 enzymes in human carbohydrate metabolism.
592 Heatmap values are the z-score $\log_2$(corrected fold change) for all metabolites in the MIDAS
593 metabolite library on a per protein basis. Clustering was performed by one minus Pearson
594 correlation. Positive (cyan) and negative (magenta) metabolite z-score $\log_2$(corrected fold change)
595 have a maximum and minimum cut-off of 10 and –10, respectively. MIDAS analysis of all proteins
596 was performed by triplicate equilibrium dialysis and technical triplicate FIA-MS injections. **(B, C,**
597 **D)** Excerpt examples of metabolite clustering from (A). Colored bars (bottom) indicate the location
598 of the extracted heatmaps from (A) (bottom). **(E)** Multidimensional scaling (MDS) of 33 human
599 enzymes in carbohydrate metabolism based on their MIDAS PMIs. MDS distance values where
600 generated from the z-score $\log_2$(corrected fold change) for all metabolites in the MIDAS
601 metabolite library on a per protein basis. **(F and G)** Significant intra-pathway (F) and inter-
602 pathway (G) interactions (colored lines) between metabolites (circles) and 33 enzymes in human
603 carbohydrate metabolism (orange boxes) (plots generated in *Electrum*). Metabolites with (light
604 grey circles) and without (dark grey circles) isomers in the same screening pool. Metabolites not
605 present in the library (open circles). Significant PMIs identified by MIDAS have a q-value < 0.01
606 and are colored by increasing significance, light orange to red.

Fig. 3

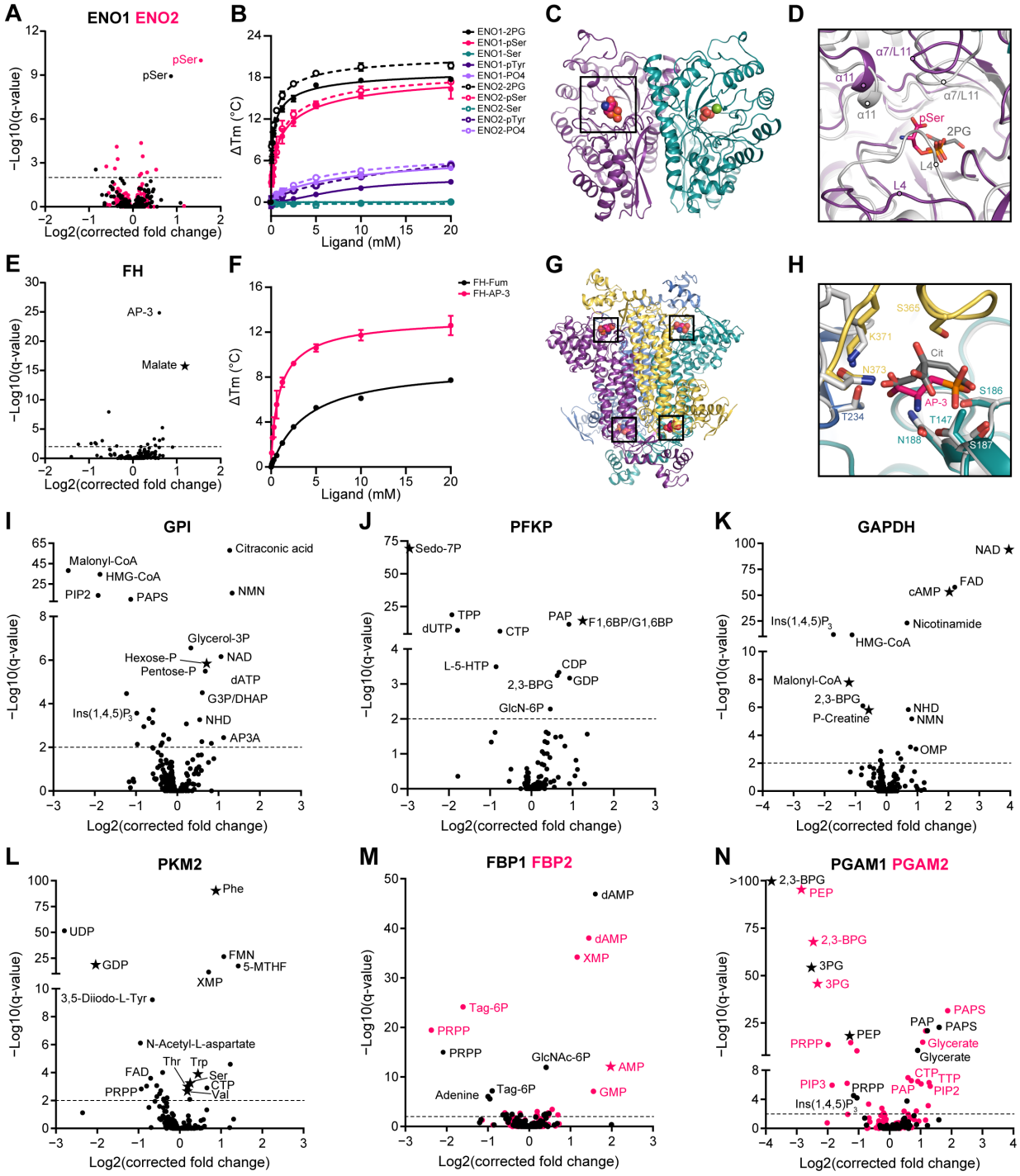
A
ENO1 ENO2
pSer
pSer
−Log10(q-value)
Log2(corrected fold change)
B
ΔTm (°C)
Ligand (mM)
ENO1-2PG
ENO1-pSer
ENO1-Ser
ENO1-pTyr
ENO1-PO4
ENO2-2PG
ENO2-pSer
ENO2-Ser
ENO2-pTyr
ENO2-PO4
C
D
α7/L11
α11
α11
α7/L11
pSer
2PG
L4
L4
E
FH
AP-3
Malate
−Log10(q-value)
Log2(corrected fold change)
F
ΔTm (°C)
Ligand (mM)
FH-Fum
FH-AP-3
G
H
S365
K371
Cit
N373
S186
AP-3
T234
T147
N188
S187
I
GPI
Citraconic acid
Malonyl-CoA
HMG-CoA
PIP2
PAPS
NMN
Glycerol-3P
Hexose-P
NAD
Pentose-P
dATP
G3P/DHAP
Ins(1,4,5)P3
NHD
AP3A
−Log10(q-value)
Log2(corrected fold change)
J
PFKP
Sedo-7P
TPP
dUTP
CTP
PAP
F1,6BP/G1,6BP
L-5-HTP
CDP
2,3-BPG
GDP
GlcN-6P
−Log10(q-value)
Log2(corrected fold change)
K
GAPDH
NAD
FAD
cAMP
Ins(1,4,5)P3
Nicotinamide
HMG-CoA
Malonyl-CoA
2,3-BPG
NHD
P-Creatine
NMN
OMP
−Log10(q-value)
Log2(corrected fold change)
L
PKM2
Phe
UDP
FMN
GDP
5-MTHF
XMP
3,5-Diiodo-L-Tyr
N-Acetyl-L-aspartate
Thr
Trp
FAD
Ser
CTP
PRPP
Val
−Log10(q-value)
Log2(corrected fold change)
M
FBP1 FBP2
dAMP
dAMP
XMP
Tag-6P
PRPP
PRPP
GlcNAc-6P
AMP
Adenine
Tag-6P
GMP
−Log10(q-value)
Log2(corrected fold change)
N
PGAM1 PGAM2
2,3-BPG
PEP
2,3-BPG
3PG
3PG
PAPS
PAP
PAPS
PRPP
PEP
Glycerate
Glycerate
CTP
TTP
PIP3
PRPP
PAP
PIP2
Ins(1,4,5)P3
−Log10(q-value)
Log2(corrected fold change)

608 **Figure 3. MIDAS identifies known and previously undescribed metabolite interactions with**
609 **enzymes from human carbohydrate metabolism.**
610 **(A)** Volcano plot of MIDAS metabolite interactions with enolase 1 (ENO1, black) and enolase 2
611 (ENO2, pink). **(B)** Ligand-induced DSF melting point analysis of ENO1 (solid lines, solid circles)
612 and ENO2 (dotted lines, open circles) with 2-phosphoglycerate (2PG, black), phosphoserine (pSer,
613 pink), serine (Ser, teal), phosphotyrosine (pTyr, purple), and phosphate (PO4, light purple). **(C)**
614 X-ray crystal structure of the pSer-ENO2 complex (PDB 7MBH). pSer (black box), phosphate ion
615 (orange and red spheres), magnesium ion (green sphere), and monomers within the ENO2 dimer
616 (purple and teal) are displayed. **(D)** Magnified view of the ENO2 active site with pSer (pink) or
617 2PG (grey) bound (2PG-ENO2, PDB 3UCC) (*53*). Secondary structure labeled in the pSer-ENO2
618 (purple) and 2PG-ENO2 (light grey) co-structures. **(E)** Volcano plot of MIDAS metabolite
619 interactions with fumarase (FH). **(F)** Ligand-induced DSF melting point analysis of FH with
620 fumarate (Fum, black) and 2-Amino-3-phosphonopropionic acid (AP-3, pink). **(B and F)** Line of
621 best fit was determined from triplicate experiments each with sextuplicate technical replicates
622 using the specific binding and Hill slope equation from GraphPad Prism 9. Mean ± SD is plotted
623 from triplicate experiments. **(G)** X-ray crystal structure of the AP-3-FH complex (PDB 7LUB).
624 AP-3 (black boxes), monomers within the FH tetramer (purple, yellow, teal, and light blue). **(H)**
625 Magnified view of the FH active site with AP-3 (pink) or citrate (Cit, grey) bound (*E. coli* Cit-FH
626 structure, light grey, PDB 1FUO) (*18*). Sidechains that coordinate the AP-3 interaction with FH
627 are labeled and colored according to FH monomer from (G). **(I – N)** Volcano plots of MIDAS
628 metabolite interactions with glucose-6-phosphate isomerase (GPI), 6-Phosphofructokinase,
629 platelet type (PFKP), glyceraldehyde-3-phosphate dehydrogenase (GAPDH), pyruvate kinase M2
630 (PKM2), fructose-1,6-bisphosphatase 1 (FBP1, black) and fructose-1,6-bisphosphatase 2 (FBP2,
631 pink), and phosphoglycerate mutase 1 (PGAM1, black) and phosphoglycerate mutase 2 (PGAM2,
632 pink). **(A, E, I – N)** Stars indicate a previously known human PMI primarily sourced from
633 BRENDA (https://www.brenda-enzymes.org/index.php). MIDAS analysis of all proteins was
634 performed by triplicate equilibrium dialysis and technical triplicate FIA-MS injections. Specific,
635 significant PMIs identified by MIDAS are labeled (See Table S1 for metabolite abbreviations).
636 Significant PMIs have a q-value < 0.01 (dotted line).

Fig. 4

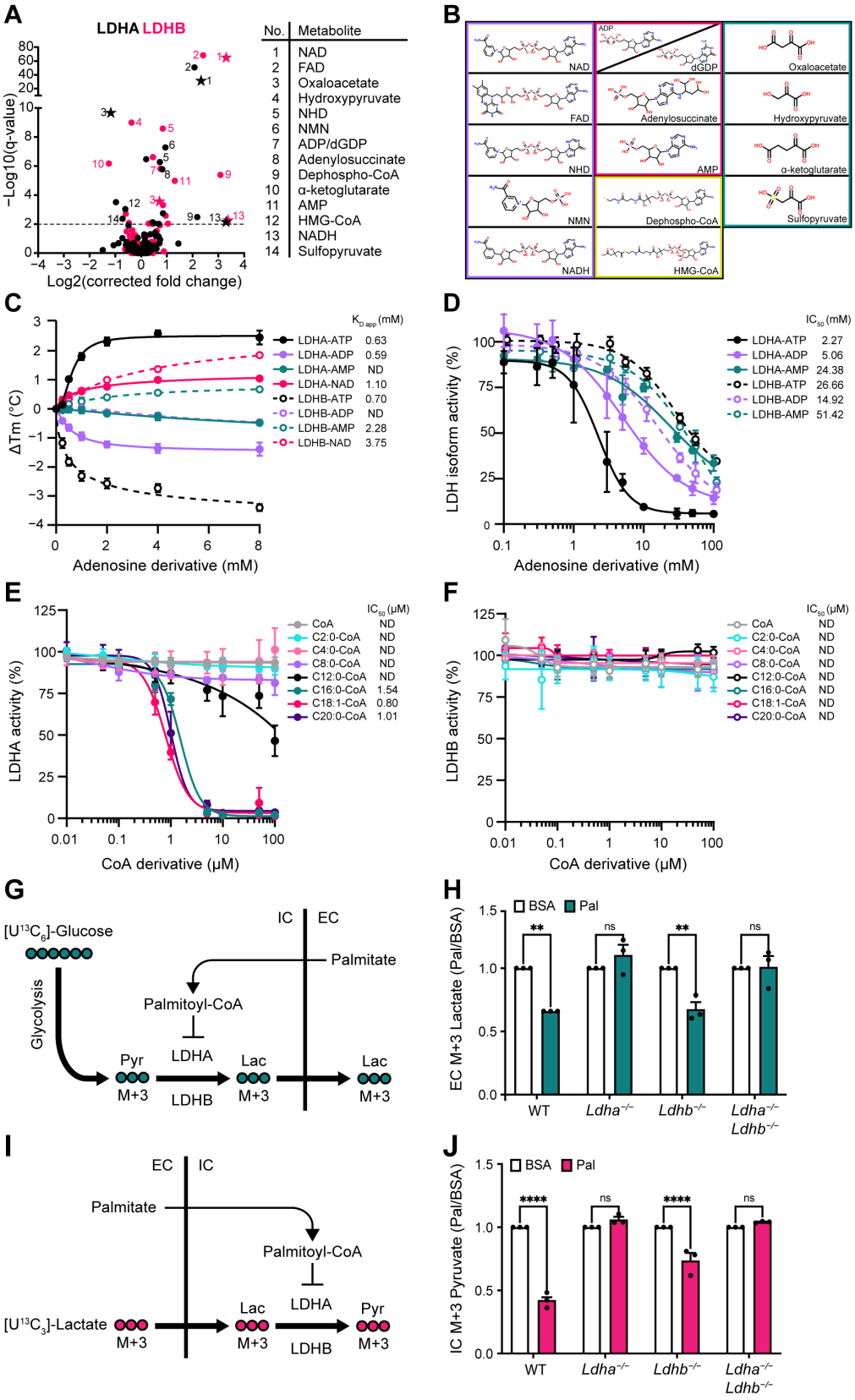
A
LDHA LDHB
−Log10(q-value)
Log2(corrected fold change)
No. | Metabolite
1 NAD
2 FAD
3 Oxaloacetate
4 Hydroxypyruvate
5 NHD
6 NMN
7 ADP/dGDP
8 Adenylosuccinate
9 Dephospho-CoA
10 α-ketoglutarate
11 AMP
12 HMG-CoA
13 NADH
14 Sulfopyruvate
B
NAD
ADP
dGDP
Oxaloacetate
FAD
Adenylosuccinate
Hydroxypyruvate
NHD
AMP
α-ketoglutarate
NMN
Dephospho-CoA
Sulfopyruvate
NADH
HMG-CoA
C
ΔTm (°C)
Adenosine derivative (mM)
K_D app (mM)
LDHA-ATP 0.63
LDHA-ADP 0.59
LDHA-AMP ND
LDHA-NAD 1.10
LDHB-ATP 0.70
LDHB-ADP ND
LDHB-AMP 2.28
LDHB-NAD 3.75
D
LDH isoform activity (%)
Adenosine derivative (mM)
IC50 (mM)
LDHA-ATP 2.27
LDHA-ADP 5.06
LDHA-AMP 24.38
LDHB-ATP 26.66
LDHB-ADP 14.92
LDHB-AMP 51.42
E
LDHA activity (%)
CoA derivative (μM)
IC50 (μM)
CoA ND
C2:0-CoA ND
C4:0-CoA ND
C8:0-CoA ND
C12:0-CoA ND
C16:0-CoA 1.54
C18:1-CoA 0.80
C20:0-CoA 1.01
F
LDHB activity (%)
CoA derivative (μM)
IC50 (μM)
CoA ND
C2:0-CoA ND
C4:0-CoA ND
C8:0-CoA ND
C12:0-CoA ND
C16:0-CoA ND
C18:1-CoA ND
C20:0-CoA ND
G
[U13C6]-Glucose
Glycolysis
IC
EC
Palmitate
Palmitoyl-CoA
LDHA
LDHB
Pyr M+3
Lac M+3
Lac M+3
H
BSA
Pal
EC M+3 Lactate (Pal/BSA)
**
ns
**
ns
WT
Ldha−/−
Ldhb−/−
Ldha−/− Ldhb−/−
I
EC
IC
Palmitate
Palmitoyl-CoA
LDHA
LDHB
[U13C3]-Lactate M+3
Lac M+3
Pyr M+3
J
BSA
Pal
IC M+3 Pyruvate (Pal/BSA)
****
ns
****
ns
WT
Ldha−/−
Ldhb−/−
Ldha−/− Ldhb−/−

638 **Figure 4. ATP and long-chain acyl-CoAs inhibit lactate dehydrogenase in an isoform-specific**
639 **manner.**
640 **(A)** Volcano plots of MIDAS metabolite interactions with lactate dehydrogenase A (LDHA, black)
641 and lactate dehydrogenase B (LDHB, pink). Specific, significant metabolites are numbered and
642 labeled. Stars indicate a previously known human PMI primarily sourced from BRENDA
643 (https://www.brenda-enzymes.org/index.php). MIDAS analysis of LDHA and LDHB was
644 performed by triplicate equilibrium dialysis and technical triplicate FIA-MS injections. Significant
645 PMIs identified have a q-value < 0.01 (dotted line). **(B)** Metabolite classes that interact with LDHA
646 and LDHB from (A) (nicotinamides and dinucleotides, purple; adenosine nucleotide derivatives,
647 pink; coenzyme A derivatives, yellow; keto acids, teal). **(C)** Ligand-induced DSF melting point
648 analysis of LDHA (solid lines, filled circles) and LDHB (dotted lines, open circles) with adenosine
649 triphosphate (ATP, black), adenosine diphosphate (ADP, light purple), adenosine monophosphate
650 (AMP, teal), and nicotinamide adenine dinucleotide (NAD, pink). Apparent dissociation constant
651 ($K_{D\ app}$) was determined from triplicate experiments each with sextuplicate technical replicates by
652 fitting the specific binding and Hill slope equation from GraphPad Prism 9. Mean ± SD is plotted
653 from triplicate experiments. **(D)** Enzyme activity of LDHA (solid lines, filled circles) and LDHB
654 (dotted lines, open circles) treated with ATP (black), ADP (light purple), or AMP (teal). **(E and**
655 **F)** Enzyme activity of LDHA or LDHB treated with coenzyme A (CoA, grey), acetyl-CoA (C2:0-
656 CoA, cyan), butyryl-CoA (C4:0-CoA, light pink), octanoyl-CoA (C8:0-CoA, light purple),
657 lauroyl-CoA (C12:0-CoA, black), palmitoyl-CoA (C16:0-CoA, teal), oleoyl-CoA (C18:1-CoA,
658 pink), and saturated arachidoyl-CoA (C20:0-CoA, purple). **(D – F)** Half maximal inhibitory
659 concentration (IC_{50}) was determined from triplicate experiments each with triplicate technical
660 replicates using GraphPad Prism 9; ND, not determined. Mean ± SD is plotted from triplicate
661 experiments. **(G)** Schematic of [$U^{13}C_6$]-glucose metabolism in cells treated with palmitate-
662 conjugated BSA following inhibition of the mitochondrial pyruvate carrier with UK5099.
663 Pyruvate, Pyr; lactate, Lac; IC, intracellular; EC, extracellular. **(H)** Fold change of extracellular
664 [$U^{13}C_3$]-lactate collected from the growth media of the indicated H9c2 cell lines in response to
665 treatment with palmitate-conjugated BSA (Pal) relative to BSA-vehicle control. Absolute
666 abundance displayed in Fig. S4H. **(I)** Schematic of [$U^{13}C_3$]-lactate metabolism in cells treated with
667 palmitate-conjugated BSA following inhibition of the mitochondrial pyruvate carrier with
668 UK5099. Pyruvate, Pyr; lactate, Lac; IC, intracellular; EC, extracellular. **(J)** Fold change of

669 intracellular [$U^{13}C_3$]-pyruvate in indicated H9c2 cell lines in response to treatment with palmitate-
670 conjugated BSA (Pal) relative to BSA-vehicle control. Absolute abundance displayed in Fig. S4J.
671 **(H and J)** Experiments were performed in triplicate and mean ± SD are displayed. A two-way
672 ANOVA and Sidak's multiple comparison test (GraphPad Prism 9) was performed between Pal
673 and BSA samples ($p < 0.005$, **; $p < 0.0001$, ****).

Supplementary Materials for

Protein-Metabolite Interactomics of Carbohydrate Metabolism Reveals Novel Regulation of Lactate Dehydrogenase.

Kevin G. Hicks[1], Ahmad A. Cluntun[1], Heidi L. Schubert[1], Sean R. Hackett[2], Jordan A. Berg[1], Paul G. Leonard[3,4], Mariana A. Ajalla Aleixo[5†], Youjia Zhou[6,7], Alex J. Bott[1], Sonia R. Salvatore[8], Fei Chang[8], Aubrie Blevins[1†], Paige Barta[1†], Samantha Tilley[1†], Aaron Leifer[1], Andrea Guzman[1], Ajak Arok[1], Sarah Fogarty[1,27], Jacob M. Winter[1], Hee-Chul Ahn[9‡], Karen N. Allen[10‡], Samuel Block[11‡], Iara A. Cardoso[5‡], Jianping Ding[12‡], Ingrid Dreveny[13‡], Clarke Gasper[14‡], Quinn Ho[14‡], Atsushi Matsuura[9‡], Michael J. Palladino[15‡], Sabin Prajapati[16,17‡], PengKai Sun[12‡], Kai Tittmann[16,17‡], Dean R. Tolan[14‡], Judith Unterlass[18‡], Andrew P. VanDemark[19‡], Matthew G. Vander Heiden[11,20‡], Bradley A. Webb[21‡], Cai-Hong Yun[22‡], PengKai Zhap[22‡], Bei Wang[6,7], Francisco J. Schopfer[8,23,24,25], Christopher P. Hill[1], Maria Cristina Nonato[5], Florian L. Muller[26], James E. Cox[1], Jared Rutter[1,27*]

Correspondance to: rutter@biochem.utah.edu

This file includes:

Materials and Methods

Figures S1 to S7

Tables S1, S2, and S3

Other Supplementary Materials for this manuscript include the following:

Data S1. MIDAS metabolite library

Data S2. FIA-MS properties of MIDAS metabolites

Data S3. MIDAS proteins

28 Data S4. MIDAS protein-metabolite interactions

Materials and Methods

MIDAS metabolite library construction and storage

The MIDAS metabolite library was constructed by extracting and cross-referencing primary and secondary metabolites from KEGG (*1*) and HMDB (*2*), with a focus on endogenous and exogenous compounds that were quantified, detected, or predicted in human metabolism (See Table S1 for metabolite abbreviations). All metabolites used in this study were purchased from Sigma-Aldrich, Cayman Chemicals, Avanti Polar Lipids, Enamine, Combi-Blocks, Inc, or custom sourced using Aldrich Market Select (Data S1). Metabolites were solvated to 10 mM in molecular grade water (Sigma-Aldrich W4502) or DMSO (Sigma-Aldrich D1435) and, where necessary to increase solubility, titrated with acid or base. The MIDAS metabolite library was arrayed 1 mL per well in 96-deep well storage plates (Greiner 780280), sealed with aluminum foil seals (VWR 60941-112), and stored at -80°C. When working stocks were needed, metabolites were moved from the deep well storage plates and arrayed, 50 µL per well, across multiple, single-use 384-well small volume storage plates (Greiner 781280), sealed with aluminum foil seals (VWR 60941-112), and stored at -80°C. Metabolite library management and manipulation was conducted on a Beckman Coulter Biomek NX^{p} SPAN-8 liquid handling robot.

MIDAS metabolite library validation and pooling

Metabolite accurate mass, adduct, ionization, and detection parameters were determined using a flow injection analysis mass spectrometry (FIA-MS) scouting approach to design four defined metabolite screening pools (Data S2, FIA-MS scout). Briefly, 20 pmol of each metabolite from the MIDAS metabolite library was independently assayed in positive and negative mode in technical quadruplicate 1 µL injections with interspersed blank injections. FIA-MS was performed on a binary pump Agilent 1290 Infinity UHPLC system operated with a flow rate of 0.1 mL/min coupled to an Agilent 6550 ESI-QTOF MS. The following mobile phases were used for FIA-MS scouting: 20 mM formic acid pH 3 (Sigma-Aldrich F0507), 10 mM ammonium acetate pH 5 (Sigma-Aldrich 73594), 10 mM ammonium acetate pH 6.8 (Sigma-Aldrich 73594), and 10 mM ammonium bicarbonate pH 9 (Sigma-Aldrich 09830). Source conditions consisted of 250°C gas temp, 11 L/min gas flow, 20 psig nebulizer, 400°C sheath gas temperature, 12 L/min sheath gas flow, and 2000 V nozzle voltage. Agilent MassHunter 7 software was used to qualitatively validate and quantify metabolites. The optimal signal for each metabolite was determined by summation

integration of the area under the counts per second trace of the extracted ion chromatogram for each metabolite adduct at the various mobile phase pH and instrument polarity. The optimal adduct, pH, polarity, metabolite solvent, and, if necessary, isomer family of each metabolite was considered to construct four unique and defined MIDAS metabolite screening pools (Data S1).

MIDAS protein-metabolite screening

The day of MIDAS screening, a number of MIDAS metabolite library 384-well small volume working stock plates, corresponding to the number of proteins to be screened (eight proteins per plate), were defrosted at 30°C for 5 minutes and metabolites were combined *de novo* to generate four predetermined MIDAS screening pools (Data S1). The MIDAS screening pools were prepared in LC-MS grade 150 mM ammonium acetate pH 7.4 (Sigma-Aldrich 73594) and pH-adjusted with ammonium hydroxide (Sigma-Aldrich 338818). The majority of metabolites were prepared to a final screening concentration of 50 µM in the metabolites pools, with a subset at higher or lower concentration dependent on their FIA-MS ionization properties (Data S1). For each metabolite pool, 8 µL of target protein (Data S3) was arrayed in a minimum of a triplicate across a 10 kDa MWCO 96-well microdialysis plate (SWISSCI Diaplate™) and sealed with aluminum foil seals (Beckman Coulter 538619) to create the protein-chambers. To the reverse side, 300 µL of metabolite pool was aliquoted per target protein replicate and sealed with aluminum foil seals (Beckman Coulter 538619) to create the metabolite-chambers. Where necessary, and just prior to screening, proteins provided in alternative buffer systems were *in situ*, sequentially exchanged into 150 mM ammonium acetate pH 7.4 (Sigma-Aldrich 73594) on the 96-well microdialysis screening plate (SWISSCI Diaplate™). Loaded dialysis plates were placed in the dark at 4°C on a rotating shaker (120 rpm) and incubated for 40 hours. Post-dialysis, protein- and metabolite-chamber dialysates were retrieved, sample volume normalized, and diluted 1:10 in 80% methanol (Sigma-Aldrich 1060351000) to denature protein, incubated 30 mins on ice, and centrifuged at 3200 x g for 15 mins to remove denatured protein. Processed protein- and metabolite-chamber dialysates were retrieved and arrayed across a 384-well microvolume plate (Thermo Scientific AB-1056), sealed with a silicon slit septum cap mat (Thermo Scientific AB-1171), and placed at 4°C for FIA-MS analysis.

MIDAS flow injection analysis mass spectrometry

91 MIDAS metabolite analyses were performed using FIA-MS, a high-throughput metabolomics
92 approach (*3-5*). Briefly, MIDAS FIA-MS was performed on a Shimadzu Nexera HPLC system
93 equipped with binary LC-20AD$_{XR}$ pumps and a SIL-20AC$_{XR}$ autosampler coupled to a SCIEX
94 X500R ESI-QTOF MS. Briefly, 2 µL of each processed protein- and metabolite-chamber dialysate
95 (~10 pmoles per metabolite, depending on metabolite) was injected in technical triplicate with
96 blanks injections interspersed between technical triplicates. Mobile phase flow rate was 0.2
97 mL/min. The following mobile phases were used according to the MIDAS metabolite pool being
98 analyzed: pool 1, 5 mM ammonium acetate pH 5 (Sigma-Aldrich 73594), 50% methanol
99 (Honeywell LC230-4); pools 2 and 4, 5 mM ammonium acetate pH 6.8 (Sigma-Aldrich 73594),
100 50% methanol (Honeywell LC230-4); pool 3, 10 mM formic acid pH 3 (Sigma-Aldrich F0507),
101 50% methanol (Honeywell LC230-4). Pools 1 and 2 were analyzed in positive mode and pools 3
102 and 4 were analyzed in negative mode. Source conditions consisted of 40 psi ion source gas 1 and
103 2, 30 psi curtain gas, 600°C source temperature, and +5500 V or -4500 V spray voltage. Method
104 duration was 1 min. All target proteins for a given metabolite pool and MS method were analyzed
105 together before switching FIA-MS methods. Between FIA-MS methods, the Shimadzu Nexera
106 HPLC system and SCIEX X500R ESI-QTOF MS where equilibrated for 40 min to the next FIA-
107 MS method. Auto-calibration of positive or negative mode was performed approximately every
108 45 mins at the beginning of a protein-metabolite pool batch to control instrument detector. Non-
109 dialyzed MIDAS metabolite pools were assayed at the beginning, middle, and end of each
110 metabolite pool method batch to monitor detector sensitivity.
111
112 <u>MIDAS data processing and analysis</u>
113 MIDAS FIA-MS spectra were processed in SCIEX OS 1.6 software using a targeted method to
114 determine metabolite abundances in the protein- and metabolite-chambers. Briefly, raw MS
115 spectra were quantitatively processed in SCIEX OS Analytics 1.6 using the MQ4 peak integration
116 algorithm to quantify metabolite abundance. Metabolite extracted ion chromatograms (XICs) were
117 identified by the intact mass determined from the chemical formula, adduct/charge, and precursor
118 mass as indicated in Data S2 with 0.01 Da XIC width, 0.16 min retention time, 2-point Gaussian
119 smooth width, 1,000 point peak splitting, and 1 min baseline subtraction window. Metabolite
120 abundance was quantified as the integrated area under the XIC counts per second peak trace.
121 Following metabolite quantification, the mean of technical triplicate injections was used to

122 generate a metabolite abundance for each protein- and metabolite-chamber per dialysis replicate.
123 If necessary, up to one dialysis replicate per pool per protein was removed if processing or
124 autosampling technical abnormalities were identified. For each dialysis replicate, log_2(fold
125 change) for each metabolite was calculated as the difference between the log_2 abundance in the
126 protein- and metabolite-chambers. Log_2(fold change) for non-seperable metabolite isomers (e.g.,
127 L-Leu/L-Ile/L-Allo-Ile, F1,6BP/G1,6BP, etc.) within the same screening pool were collapsed to a
128 single entry prior to further data processing leading to 333 unique metabolite analytes (isomer
129 entries delimited by "/"). Using the replicate protein-metabolite log2(fold change) values as input,
130 a processing method was developed in R (https://github.com/KevinGHicks/MIDAS) to filter
131 extreme outliers, correct for non-specific systematic variation and to identify significant protein-
132 metabolite interactions. Briefly, for each dialysis triplicate set, the mean and standard deviation
133 were used to generate z-scores, and up to one outlier was removed using a z-score cutoff of five
134 (<0.2% of observations). Dialysis replicates were then averaged yielding one mean fold change
135 summary per protein-metabolite pair. To remove fold change variation that was not specific to a
136 given protein-metabolite pair, the first three principal components of the total screening dataset
137 were removed on a per metabolite pool basis by subtracting the projection of the first three
138 principal components, creating log2(corrected fold change). This approach is similar to commonly
139 used methodologies such as surrogate variable analysis (*6, 7*) that correct for latent variables
140 explaining a large amount of variance in a dataset which is not captured by experimental
141 covariates. PMIs were identified as extreme fold changes relative to each metabolite's variation
142 across all 158 unique proteins analyzed (36 proteins presented in this study, in addition to 122
143 anonymized proteins). Across proteins, a metabolite's fold change distribution is a mixture of non-
144 PMIs (which are approximately normally-distributed) and genuine PMIs, which tend to have
145 extreme fold changes. Ideally, we would want to compare each putative PMI to a background
146 distribution of non-PMIs but since these classes are unknown we can instead assume that no
147 metabolite interacts with most proteins and estimate summaries of the overall fold change
148 distribution which should approximate the non-PMI's "no-signal" variability. To do this we
149 calculate a z-score by comparing each protein-metabolite log2(corrected fold change) to a a no-
150 signal model for that metabolite using measures of the central tendency (median) and standard
151 deviation (extrapolated from the inter quartile range (IQR); i.e., $\boldsymbol{\sigma}$ = IQR/1.35 based on the
152 standard properties of the Normal distribution), which are robust to the signals in the tails of a

153 metabolite's fold change distribution. When signals do exist, the IQR method will overestimate
154 the standard deviation, hence the method is statistically conservative. Protein-metabolite
155 interaction z-scores were compared to the quantiles of the standard Normal distribution to generate
156 p-values and were false-discovery rate controlled using Storey's q-value (*8*). Protein-metabolite
157 interactions with q-values < 0.01 were considered significant for subsequent analyses. The
158 complete MIDAS protein-metabolite interaction dataset for mTORC1 regulators and enzymes of
159 carbohydrate metabolism can be found in Data S4.
160
161 Comparison of MIDAS PMIs to external databases
162 All activators and inhibitors of E.C.-associated MIDAS proteins were obtained from BRENDA
163 using their SOAP API (*9*). BRENDA ligand identifiers were matched to ChEBI identifiers using
164 UniChem (*10*). Reactants were defined as the substrates and products of a reaction catalyzed by a
165 specific enzyme as defined in Recon3D (*11*). Recon3D metabolite ChEBI annotations and
166 enzymes were matched from Entrez to E.C. using the bioconductor org.Hs.eg.db package
167 (Carlson M (2019). org.Hs.eg.db: Genome wide annotation for Human. R package version
168 3.8.2.). BRENDA and Recon3D reports were reduced to one entry per protein-metabolite pair
169 prioritizing reactants from Recon3D for instances where a protein-metabolite pair is present as a
170 substrate in Recon3D and as a regulator in BRENDA. MIDAS protein-metabolite interactions
171 were matched to BRENDA and Recon3D reports based on shared E.C. numbers and ChEBI
172 identifiers. When a MIDAS protein matched multiple E.C. numbers or a MIDAS metabolite
173 matched multiple ChEBI IDs, only a single entry per measured protein-metabolite pair was
174 retained, prioritizing reactants over regulators and regulators over protein-metabolite interactions
175 unreported in BRENDA or Recon3D. Statistical significance was determined by performing a
176 2x2 Fisher's exact test on annotated MIDAS substrates and products or activators and inhibitors
177 relative to MIDAS PMIs unreported in BRENDA and Recon3D.
178
179 MIDAS proteins
180 All presented proteins analyzed by MIDAS were prepared and provided by collaborators using
181 common protein expression and purification techniques (Data S3). Proteins were received snap
182 frozen on dry ice from outside sources or on wet ice from local sources and screened immediately
183 upon defrost. Prior to MIDAS screening, protein quality was assessed by 12.5% SDS-PAGE and

concentration was determined by A280 on a NanoDrop One UV-Vis spectrophotometer using the molecular weight and extinction coefficient ($M^{-1} \cdot cm^{-1}$) of each protein construct. Proteins were screened by MIDAS at the concentrations indicated in Data S3.

Electrum

MIDAS protein-metabolite interaction data for enzymes of carbohydrate metabolism were visualized for intra- and inter-pathway relationships using the publicly available MIDAS data visualization tool, *Electrum*, developed for this study (v0.0.0; https://github.com/Electrum-app/Electrum/releases/tag/v0.0.0), with q-value cutoff < 0.01, and the 1-D scaling option enabled.

Electrum: database formatting

For a given protein-metabolite interaction database for evaluation in *Electrum*, each row of the database should represent a given protein-metabolite interaction. This database should be exported as a tab-delimited file. For each interaction, the metabolite common name and target protein name abbreviation should be given, along with the log2(fold change), p-value, and log2(corrected fold change) and q-values as determined by the MIDAS data processing method (https://github.com/KevinGHicks/MIDAS).

Electrum: metadata curation and integration

A Reactome human metabolic network database (*12-14*) is built by metaboverse-cli (*15*) by extracting relevant human pathway and reaction dictionaries that act as metadata within various *Electrum* visualization options (https://reactome.org/download/current/all_species.3.1.sbml.tgz). Pathway dictionaries list all reactions annotated within each pathway and reaction dictionaries list the metabolites and other components of each reaction. Databases of protein and metabolite synonyms are output using *Electrum's* Python utility, "make_entity_dictionary".

Electrum: graph generation

An *Electrum* graph is generated using the MIDAS protein-interaction database. For each protein-metabolite interaction, an edge is added with the fold change and statistical values as edge attributes. If a node does not yet exist in the graph for the metabolite and/or protein, one is added. Metabolite and protein synonyms are also added to each node to ensure correct mapping. Database

215 import and graph generation are performed using D3 (https://d3js.org/). Single-clicking on a
216 metabolite node will display the pathways and reactions that metabolite is known to participate in
217 based on the Reactome knowledgebase information for the human metabolic network (*12-14*) as
218 curated by metaboverse-cli as a ".eldb" database (*15*). Double-clicking on a metabolite node will
219 link the user to the Human Metabolome Database (HMDB) (*2*) to enable users to explore this
220 resource for further information regarding that metabolite. Users can set the q-value threshold to
221 determine which protein-metabolite interactions to display for a given protein or pathway. Users
222 can also export a generated protein-metabolite graph as a SVG file.
223
224 *Electrum*: edge weighting
225 Edge weights are represented visually using either a combination of the corrected fold changes
226 and q-values ("2-D Scaling") or the q-values alone ("1-D Scaling"). "2-D Scaling" scales the edge
227 width by interaction q-value and the edge color hue by interaction correct fold change. "1-D
228 Scaling" scales edge color hue by interaction q-value and all edge widths are uniform.
229
230 *Electrum*: pathway and interaction visualization
231 At the time of writing, *Electrum* users have three primary visualization methods, which are
232 described below:
233 1. Single target protein interaction network: A user selects a given protein target that has been
234 assayed by MIDAS. All protein-metabolite interactions passing the selected q-value
235 threshold are then displayed.
236 2. Intra-pathway interaction network: A user selected a curated metabolic pathway and all
237 proteins from that pathway are displayed. All metabolite interactions involving this
238 pathway's proteins are also displayed if they have been canonically annotated to belong to
239 this pathway.
240 3. Inter-pathway interaction network: A user selected a curated metabolic pathway and all
241 proteins from that pathway are displayed. All metabolite interactions involving this
242 pathway's proteins are also displayed whether they have been canonically annotated to
243 belong to this pathway.
244
245 *Electrum*: code availability

246 The source code for *Electrum* is available at https://github.com/Electrum/Electrum-app under a
247 GPL-3.0 license. *Electrum* relies on the following dependencies: D3 (v5.16.0) (https://d3js.org/),
248 d3-ForceEdgeBundling (https://github.com/upphiminn/d3.ForceBundle), JQuery (v3.5.1)
249 (https://jquery.com/), saveSvgAsPng (v1.4.17) (https://github.com/exupero/saveSvgAsPng),
250 streamsaver (v2.0.5) (https://github.com/jimmywarting/StreamSaver.js), Reactome (v75) (*12-*
251 *14*), and Metaboverse (v0.4.0b) (*15*).
252
253 Differential scanning fluorimetry
254 Thermal differential scanning fluorimetry (DSF) was performed similar to Niesen *et al.* (*16*).
255 Briefly, DSF thermal shift assays were developed to assess protein melting point (Tm) and thermal
256 stability in the presence of putative small molecule ligands: 2-phosphoglycerate (Sigma-Aldrich
257 73885), phosphoserine (Sigma-Aldrich P0878), phosphotyrosine (Sigma-Aldrich P9405),
258 phosphate (Acros Organics 424395000), fumarate (Sigma-Aldrich 47910), 2-amino-3-
259 phosphonopropionic acid (Sigma-Aldrich A4910), ATP (Sigma-Aldrich A2383), ADP (Sigma-
260 Aldrich 01905), AMP (Sigma-Aldrich A2252), NAD (Sigma-Aldrich N1636), and palmitoyl-CoA
261 (Avanti 870716). Where indicated, DSF experiments were performed using either the standard
262 SYPRO orange fluorescent system or PROTEOSTAT® Thermal shift stability assay kit (ENZO
263 51027). A final concentration reaction mixture of 10 µL containing 25 mM HEPES pH 7.4, 50
264 mM NaCl, 0.1 mg/mL (SYPRO system) or 0.75 mg/mL (PROTEOSTAT system) target protein,
265 7.5X SYPRO orange (Sigma-Aldrich S5692) or 1x PROTEOSTAT® reagent, and the indicated
266 concentration of putative ligand was arrayed across a MicroAmp™ optical 384-Well reaction plate
267 (Thermo Scientific 4309849) and sealed with MicroAmp™ optical adhesive film (Thermo
268 Scientific 4360954). Protein denaturation was measured in sextuplicate technical replicates for
269 SYPRO orange and PROTEOSTAT experiments with an excitation of 470 nm and emission of
270 580 nm on an Applied Biosystems Quantstudio 7 Flex from 25°C to 95°C at a ramp rate of
271 0.05°C/second. DSF experiments were performed in triplicate. Protein Thermal Shift software 1.4
272 (Applied Biosystems) was used to interpret and determine protein Tm from the first derivative of
273 the fluorescence emission as a function of temperature (dF/dT). A change in ligand-induced
274 protein melting point (ΔTm) was determined from the difference of the ligand induced Tm and no-
275 ligand control Tm. Apparent binding affinity ($K_{D\ app}$) was determined by fitting the specific binding

276 and Hill slope equation to ΔTm as a function of ligand concentration in GraphPad Prism 9
277 software.
278
279 Fumarase competitive inhibition assay
280 The competitive inhibition of human fumarase activity in the presence of 2-amino-3-
281 phosphonopropionic acid (Sigma-Aldrich A4910) was fluorometrically assessed using a coupled
282 enzyme assay. Briefly, the rate limiting hydration of fumarate to malate by fumarase provides
283 substrate, malate, for excess malate dehydrogenase to generate oxalacetate and NADH. Fumarase
284 reaction rate was assessed at room temperature in triplicate with a final reaction volume of 100 µL
285 composed of 50 mM Tris-HCl pH 9.4, 0.61 ng/µL human fumarase, excess porcine heart malate
286 dehydrogenase (Sigma-Aldrich 442610-M), 1 mM NAD (Sigma-Aldrich N1636), and varying
287 concentrations of fumarate (0 – 40 mM, Sigma-Aldrich 47910) and AP-3 (0 – 10 mM, Sigma-
288 Aldrich A4910). Fumarate and 2-amino-3-phosphonopropionic acid were added simultaneously.
289 The production of NADH was quantified fluorometrically in a black, clear bottomed 96-well plate
290 (Sigma-Aldrich CLS3603) on a Biotek Synergy Neo plate reader with 360 nm excitation and 460
291 nm emission over 10 minutes and fumarase reaction rate was determined from the linear range of
292 increasing NADH signal. A Lineweaver-Burke linear regression and non-linear regression
293 competitive inhibition model of human fumarase between fumarate and 2-amino-3-
294 phosphonopropionic acid were fit using GraphPad Prism 9 software from triplicate competitive
295 inhibition experiments.
296
297 Enolase 2 Activity Assay
298 Human enolase 2 (ENO2) activity was measured in the presence of phosphoserine using a coupled
299 enzyme kinetic assay similar to Satani *et al.* (*17*). Briefly, enolase converts 2-phosphoglycerate to
300 phosphoenolpyruvate and water. Substrate, 2-phosphoglycerate, was provided near the measured
301 Km. Excess pyruvate kinase (PK) / lactate dehydrogenase (LDH) enzymes from rabbit muscle
302 (Sigma P0294), ADP, NADH were added to solution to ensure that dehydration of 2-
303 phosphoglycerate by enolase was the rate-limiting step. Enolase reaction rate was assessed at room
304 temperature in triplicate with a final reaction volume of 100 µL composed of 50 mM HEPES pH
305 7.4, 0.5 mM MgCl2, 100 mM NaCl, 1.75 mM ADP, 200 µM NADH, 12.8 U PK, 18.4 U LDH,
306 0.625 ng/µL ENO2, 30 µM 2PG, with varying concentrations of phosphoserine. 2-

307 phosphoglycerate was used to initiate the coupled enzyme reaction, and the conversion of NADH
308 to NAD by LDH was quantified fluorometrically in a black, clear bottomed 96-well plate (Sigma-
309 Aldrich CLS3603) on a Biotek Synergy Neo plate reader with 360 nm excitation and 460 nm
310 emission over 10 minutes. Enolase reaction rate was determined for the linear range of decreasing
311 NADH signal. IC50 was determined using a sigmoidal, 4PL non-linear regression in GraphPad
312 Prism 9 from triplicate experiments each with technical reaction triplicates.
313
314 Enolase X-ray crystallography
315 Crystals of human enolase 2 in complex with the phosphoserine ligand were prepared via hanging
316 drop vapor diffusion at 20 °C. 9 mg/ml human enolase 2 protein solution with 2 mM phosphoserine
317 was pre-incubated on ice for 10 min prior to being mixed in 1:1 ratio (protein:reservoir solution)
318 with 100 mM Bis Tris, 200 mM ammonium acetate and 21% (w/v) PEG 3350 at pH 6.5.
319 Orthorhombic crystals grew within 3 days and were subsequently cryoprotected with 100 mM Bis
320 Tris, 200 mM ammonium acetate, 32% (w/v) PEG 3350 and 2 mM phosphoserine. X-ray
321 diffraction data were collected at the Advanced Photon Source, synchrotron beamline 22-ID,
322 equipped with Si(III) monochromator and EIGER CCD detector. The diffraction data was
323 processed and integrated using iMOSFLM (*18*). POINTLESS (*19*) was used to identify the bravais
324 lattice and space group and AIMLESS (*20*) was used for scaling. The phase information was
325 obtained by molecular replacement using PHASER (*21*) with a homodimer of human enolase 2
326 (PDB 4ZCW) as the search model. Iterative cycles of manual model building and refinement were
327 performed within Phenix (*22*) and COOT (*23*) software. Diffraction data and refinement statistics
328 are summarized in Table S2.
329
330 Fumarase X-ray crystallography
331 Human fumarase was produced and purified as previously described (*24*). The co-crystallization
332 experiments were carried out by using the sitting drop method. Protein solution (4 mg/mL in 50
333 mM Tris-HCl (Sigma-Aldrich), pH 8.5, 150 mM KCl (J.T.Baker) was incubated with 20 mM of
334 2-amino-3-phosphonopropionic acid (Sigma-Aldrich A4910). 2 µL of protein solution was mixed
335 with 2 µL of reservoir solution, and allowed to equilibrate against 500 µl of reservoir solution at
336 21°C. Crystals occur over the course of 3 days in drops where the reservoir contained 100 mM
337 Hepes pH 7.5 (Sigma-Aldrich), 1% v/v 2-methylpentanediol (MPD) (Sigma-Aldrich) and 18%

338 (w/v) PEG 10 K (Sigma-Aldrich) and 25% (v/v) glycerol. Prior to data collection, HsFH crystals
339 were soaked in a cryoprotectant solution (100 mM Hepes pH 7.5, 1% v/v 2-methylpentanediol
340 (MPD), and 18% m/v PEG 10 K, 25% v/v glycerol (Labsynth), harvested with cryo loops, and
341 flash-cooled in liquid nitrogen. The data set was collected at 100 K on a synchrotron facility
342 (MANACA beamline - SIRIUS, Brazil) using a PILATUS 2M detector (Dectris). 3600 frames
343 with an oscillation step of 0.1° were collected using an exposure time of 0.1 s per image with a
344 crystal-to-detector distance of 120.05 mm. The images of X-ray diffraction were processed with
345 XDS (*25*) package, and the structure of HsFH was solved by molecular replacement implemented
346 in Molrep (*26*) program, and using the human fumarase structure (PDB 5UPP) (*24*) as a template.
347 The structure was refined with Refmac5 (*27*) intercepted with manual map inspection and model
348 building using Coot (*23*). The quality of the model was regularly checked using MolProbity (*28*).
349 Diffraction data and refinement statistics are summarized in Table S3. The refined atomic
350 coordinates and structure factors were deposited in the PDB with the accession code 7LUB.
351
352 Lactate dehydrogenase activity assay
353 Human lactate dehydrogenase A (LDHA) and lactate dehydrogenase B (LDHB) activity were
354 assessed in the presence of nucleotides and fatty acyl-CoAs using a standard NADH fluorometric
355 assay. Briefly, lactate dehydrogenase reversibly converts lactate and NAD to pyruvate and NADH.
356 With the exception of the competitive inhibition assay, LDHA and LDHB activity assays were
357 operated near the measured Km values of their substrates and cofactors. Lactate dehydrogenase
358 reaction rate was assessed at room temperature in triplicate with a final reaction volume of 100 µL
359 composed of 75 mM Tris pH 7.4, 67.2 ng/ml LDHA or 75 ng/mL LDHB, 6.5 mM lactate (Sigma-
360 Aldrich L6402) and 200 µM NAD (Sigma-Aldrich N1636) for LDHA and 1mM lactate and 1.25
361 mM NAD for LDHB, with varying concentrations of putative ligand, as indicated: ATP (Sigma-
362 Aldrich A2383), ADP (Sigma-Aldrich 01905), AMP (Sigma-Aldrich A2252), CoA (Avanti
363 870701), C2:0-CoA (Avanti 870702), C4:0-CoA (Avanti 870704), C8:0-CoA (Avanti 870708),
364 C12:0-CoA (Avanti 870712), C16:0-CoA (Avanti 870716), C18:1-CoA (Avanti 870719), and
365 C20:0-CoA (Avanti 870720). For competitive inhibition assay, the concentrations of lactate or
366 NAD were varied, accordingly. Unless indicated otherwise, NAD was used to initiate the LDH
367 reaction. For LDH IC_{50} assays utilizating 2,2-dimethyl-palmitoyl-CoA (DiMePal-CoA), the
368 protein concentrations and reaction buffer were the same as above except 60 µM sodium pyruvate

369 (Sigma Aldrich P2256) was used as substrate and 20 µM NADH (Sigma-Aldrich 10107735001)
370 was used to initiate the reaction. The production or depletion of NADH was quantified
371 fluorometrically in a black, clear bottomed 96-well plate (Sigma-Aldrich CLS3603) on a Biotek
372 Synergy Neo plate reader with 360 nm excitation and 460 nm emission over 10 minutes and lactate
373 dehydrogenase reaction rate was determined from the linear range of increasing or decreasing
374 NADH signal. IC_{50} were determined using a sigmoidal, 4PL non-linear regression in GraphPad
375 Prism 9 from triplicate experiments each with technical reaction triplicates. Non-linear regression
376 competitive or non-competitive inhibition modeling of LDHA between lactate or NAD and ATP
377 or palmitoyl-CoA were fit using GraphPad Prism 9 software from triplicate experiments.
378
379 Palmitoyl-CoA-Agarose pull-down assay
380 LDHA and LDHB interaction with palmitoyl-CoA was assessed using a pull-down, competitive
381 elution assay. Briefly, 30 µL per pull-down of palmitoyl-CoA conjugated agarose beads (Sigma-
382 Aldrich 5297) were buffer exchanged into pull-down buffer (75mM Tris HCl pH 7.4). In a final
383 volume of 300 µL, 0.2 mg/mL of LDHA or LDHB protein were combined with buffer exchanged
384 palmitoyl-CoA agarose beads, a loading control was saved, and the mixture was incubated
385 overnight at 4°C with gentle agitation. Post-incubation, pull-down reactions were washed 5 times
386 in 100 µL of pull-down buffer and the final wash was saved for analysis. Following the fifth wash,
387 100 µM of acetyl-CoA or palmitoyl-CoA or equivalent volume of pull-down buffer were added to
388 the reactions and incubated overnight at 4°C. In the morning, the pull-down reactions were
389 centrifuged to pellet beads, the supernatant was collected and concentrated as the eluate fraction,
390 the beads were collected as the bound fraction. All samples were boiled for 5 minutes in 4x
391 Laemmli sample buffer and analyzed by SDS-PAGE.
392
393 Tissue culture
394 H9c2 myoblastic cell line (ATCC CRL-1446) was purchased from ATCC and routinely
395 maintained in DMEM media supplemented with 10% FBS and 1% PenStrep in 5% CO2 and 37°C.
396 Third passage H9c2 cells were used for experimentation and mutant cell line generation.
397
398 *Ldha* and *Ldhb* mutant cell lines
399 $Ldha^{-/-}$, $Ldhb^{-/-}$, and $Ldha^{-/-}$ $Ldhb^{-/-}$ knock out H9c2 cell lines were generated using CRISPR-
400 Cas9 to excise the first coding exon of each gene. Single guide modified synthetic sgRNAs were

401 obtained from Synthego and Hifi-Cas9 was obtained from IDT (cat# 1081060). Pairs of
402 ribonucleoprotein (RNP) complexes targeting upstream and downstream of the first coding exon
403 for each gene were co-electroporated using a Lonza 4D Nucleofector system
404 (https://knowledge.lonza.com/cell?id=1016&search=H9c2). The N20 sgRNA target sequences
405 used were GAGTGCAACGCTCAACGCCA and TCCACAGGCTTGTGACATAA for *Ldha* and
406 TCCATGCATGTAAAGCACAT and AAGACAGCACAACTCTATAG for *Ldhb*. Off-targets
407 for these sgRNAs were screened using CasOT (*29*). Nucleofected cells were plated as single clones
408 and clones were screened for the expected genomic deletion and presence of the WT allele using
409 PCR. Additionally, $Ldha^{-/-}$, $Ldhb^{-/-}$, and $Ldha^{-/-}$ $Ldhb^{-/-}$H9c2 cells were confirmed at the
410 protein level by Western blot (see Cell lysate and western blotting).
411
412 Cell lysate and western blotting
413 Harvested cells were washed with PBS and lysed in RIPA buffer (50 mM Tris, 150 mM NaCl,
414 0.1% SDS, 0.5% sodium deoxycholate, 1% NP-40) supplemented with protease and phosphatase
415 inhibitors. Protein concentration was quantified with the Pierce BCA Protein Assay Kit. Samples
416 were mixed with 4x sample loading buffer and incubated for 5 min at 95°C. 30 µg of total protein
417 lysate was resolved by SDS-PAGE according to standard procedure at 20 mA per gel and blotted
418 onto a nitrocellulose membrane 0.45 µm (GE Healthcare) via Mini Trans-blot module (Bio-Rad)
419 at a constant voltage (100 V) for 2 h. After blocking with 5% non-fat milk (Serva)/Tris-buffered
420 saline with 0.05% Tween 20 (TBS-T) for 1 hour, the membrane was incubated overnight in 5%
421 bovine serum albumin (Sigma-Aldrich), TBS-T with primary antibody against LDHA (Cell
422 Signaling Technology 2012S, 1:1000), LDHB (Abcam ab240482, 0.1 g/ml), and GAPDH (Cell
423 Signaling Technology 97166, 1:1000). Next day, the membrane was washed with TBS-T and
424 incubated with corresponding fluorophore-conjugated secondary antibody (Rockland
425 Immunochemical RL611-145-002, 1:10000) in 1% non-fat milk/TBS-T for 1 hour. The membrane
426 was then washed again with TBS-T and fluorescence was assessed with Odyssey CLx imaging
427 system (LI-COR Biosciences).
428
429 Synthesis of 2,2-dimethyloctadecanoic acid (2,2-dimethylstearic acid)
430 To a solution of 1-bromohexadecane (1.0 g, 3.3 mmol) and ethyl isobutyrate (380 mg, 439 µL,
431 3.28 mmol) in THF (20 mL) was slowly added lithium diisopropylamide (2M in THF, 2.6 mL, 5.2

mmol) at -78°C. The reaction mixture was slowly warmed to rt and stirred for 18h. It was then quenched with ice-cooled 1N HCl. The resulting mixture was extracted with ethyl acetate three times. The organic layers were combined, dried, and evaporated. The crude product was purified by a SiO_2 column (0-10% ethyl acetate in hexanes) to give the desired ethyl 2,2-dimethyloctadecanoate (805 mg, 72%) as a colorless oil. To a solution of ethyl 2,2-dimethyloctadecanoate (751 mg, 2.21 mmol) in THF (12 mL), H_2O (3 mL), and MeOH (3 mL) was added lithium hydroxide (559 mg, 23.3 mmol). The mixture was stirred at 55°C for 48 h. The reaction was then quenched with ice-cooled 1N HCl and extracted with dichloromethane three times. The organic layers were combined, dried, and evaporated. The crude product was purified by a SiO_2 column (0-15% ethyl acetate in hexanes) to give the desired product as a white solid (423 mg, 61%). ^{1}H NMR ($CDCl_3$, 300MHz): δ 1.52 (m, 2H), 1.25 (m, 28H), 1.19 (s, 6H), 0.88 (t, *J*=7Hz, 3H). ^{13}C NMR ($CDCl_3$, 75MHz): δ 14.1, 22.7, 24.8, 24.9, 29.4, 29.5, 29.6, 29.7, 29.7, 30.1, 32.0, 40.6, 42.1, 184.5.

<u>Synthesis of 2,2-dimethylhexadecanoic acid (2,2-dimethylpalmitic acid)</u>

To a solution of 1-bromotetradecane (1.174 g, 4.238 mmol) and ethyl isobutyrate (590 mg, 682 μL, 5.09 mmol) in THF (20 mL) was slowly added lithium diisopropylamide (2M in THF, 4.24 mL, 8.48 mmol) at 0°C. The reaction mixture was slowly warmed to rt and stirred for 5h. It was then quenched with ice-cooled 1N HCl. The resulting mixture was extracted with ethyl acetate three times. The combined organic layers were then washed with a saturated NH_4Cl solution twice. The organics were dried and evaporated. The crude product was hydrolyzed directly without further purification. To a solution of the aforementioned crude ethyl 2,2-dimethylhexadecanoate in THF (10 mL), H_2O (3 mL), and MeOH (3 mL) was added lithium hydroxide (1.02 g, 42.5 mmol). The mixture was stirred at 55°C for 48 h. The reaction was then quenched with ice-cooled 1N HCl and extracted with ethyl acetate three times. The organic layers were combined, dried, and evaporated. The crude product was purified by a SiO_2 column (0-15% ethyl acetate in hexanes). For additional purification, the resulting product was then dissolved in a 1M KOH solution. The aqueous phase was washed with ethyl acetate twice and then acidified with a 1N HCl solution. The resulting suspension was extracted with ethyl acetate three times. The combined ethyl acetate layers were dried and evaporated to give the purified 2,2-dimethylhexadecanoic acid as a white crystal (470 mg, 39%). ^{1}H NMR ($CDCl_3$, 300MHz): δ 1.55 (m, 2H), 1.28 (m, 24H), 1.21 (s, 6H),

463 0.90 (t, *J*=7Hz, 3H). ^{13}C NMR ($CDCl_3$, 75MHz): δ 14.1, 22.7, 24.8, 24.9, 29.4, 29.5, 29.6, 29.7,
464 29.7, 30.1, 31.9, 40.6, 42.1, 184.6.
465
466 Synthesis of the 2,2-dimethylpalmitoyl-CoA conjugate
467 The synthesis and purification of fatty acid-CoA conjugates were modified based on reported
468 methods (*30-32*). To a solution of 2,2-dimethylpalmitic acid (100 mg, 0.352 mmol) in DCM (5
469 mL) was added N,N'-carbonyldiimidazole (114 mg, 0.703 mmol). The mixture was stirred at rt for
470 2h until the acid was consumed. The reaction mixture was then repeatedly washed with water (5
471 mL×4) until the organic layer was no longer cloudy. The organic layer was dried and evaporated
472 to give the crude 1-(1H-imidazol-1-yl)-2,2-dimethylhexadecan-1-one. To this crude product in
473 THF (5 mL) was added Coenzyme A hydrate (40 mg, 0.052 mmol) in a 0.1 M $NaHCO_3$ aq. solution
474 (5 mL). The mixture was stirred at rt for 18h before quenched with an HCl solution (pH=1, 5 mL).
475 The crude fatty acid-CoA conjugate was precipitated upon the addition of ethyl acetate (~5 mL).
476 The suspension was filtered, and the solid was washed with acetone (10 mL×2) and ethyl acetate
477 (10 mL×2) to give the desired 2,2-dimethylpalmitic acid-CoA conjugate as a white solid (12 mg,
478 22%). ^1H NMR (DMSO-*d6*, 400MHz): δ 8.57 (s, 1H), 8.31 (s, 1H), 8.12 (t, *J*=6Hz, 1H), 7.76 (t,
479 *J*=6Hz, 1H), 5.98 (d, *J*=5.4Hz, 1H), 4.80 (m, 1H), 4.71 (m, 1H), 4.38 (m, 1H), 4.16 (m, 2H), 3.90
480 (m, 1H), 3.75 (s, 1H), 3.70-3.43 (br, H_20), 3.33-3.10 (m, 4H), 2.85 (t, *J*=7Hz, 2H), 2.25 (t, *J*=7Hz,
481 2H), 1.48 (m, 2H), 1.22 (bm, 24H, 1.13 (s, 6H), 0.95 (s, 3H), 0.85 (t, *J*=7Hz, 3H), 0.73 (s, 3H).
482 HRMS m/z calcd for $C_{39}H_{71}N_7O_{17}P_3S^+$ $[M+H]^+$: 1034.3835, found 1034.3803.
483
484 Metabolite extraction
485 The procedures for metabolite extraction from cultured cells are described in previous studies (*33-*
486 *35*). Briefly, adherent cells were grown in 10 cm plates in biological triplicate to 80% confluence,
487 medium was rapidly aspirated and cells were washed with cold 0.9% NaCl TC grade (Sigma-
488 Aldrich S8776-100ML) on ice. 3 ml of extraction solvent, 80% (v/v) LC/MS grade methanol/water
489 (Fisher Scientific W6-1, A456-1) cooled to −80°C, was added to each well, and the dishes were
490 transferred to −80°C for 15 min. Cells were then scraped into the extraction solvent on dry ice.
491 Additionally, 300 mL of media was collected and processed from each sample pre and post
492 experiment. All metabolite extracts were centrifuged at 20,000 x g at 4°C for 10 min. Each sample

493 was transferred to a new 1.5 mL tube. Finally, the solvent in each sample was evaporated in a
494 Speed Vacuum, and stored at −80°C until they were run on the mass spectrometer.
495
496 [U-$^{13}C_6$]-Glucose and [U-$^{13}C_3$]-Lactate labeling with or without palmitate, dimethyl-palmitate or
497 dimethyl-stearate
498 H9c2 cells were grown to 80% confluence in 10 cm plates with standard culture medium at which
499 point 10 µM of the MPC inhibitor UK5099 (Sigma-Aldrich PZ0160-5MG) was added for 48 hours
500 to facilitate lactate production. Cells were subsequently washed with sterile PBS and either free
501 BSA, BSA conjugated to palmitate (Caymen Chemical 29558), or BSA conjugated to either 2,2-
502 dimethyl-palmitate (DiMePal) or 2,2-dimethyl-stearate (DiMeSte) was added to culture media
503 containing either [U-$^{13}C_6$]-L-glucose, or [U-$^{13}C_3$]-L-lactate (Cambridge Isotope Laboratories
504 CLM-1396, CLM-1579-PK), supplemented with dialyzed Fetal Bovine Serum (Thermo Scientific
505 A3882001) and incubated for 4 hours. Metabolites were extracted as described above. Data was
506 corrected for naturally occurring ^{13}C isotope abundance before analysis as described in Buescher
507 *et al.* (*51*). All data expressed as mean ± SD unless otherwise indicated. Student's t test was used
508 for 2 group comparison. One-Way ANOVA and Sidak's comparisons were used for multigroup
509 comparison. $p < 0.05$ were considered statistically significant. Statistical analyses and graphics
510 were carried out with GraphPad Prism 9 software. Tracing experiments were performed in
511 triplicate.
512
513 Triacsin C experiments
514 Triascin C experiments were performed as previously reported (*36*), briefly H9c2 cells were
515 pretreted with UK5099 and grown in 100 µM of BSA-conjugated palmitate for 24 hours before
516 being treated with 5 µM of Triacsin C for another 24 hours. Cells were then washed with PBS and
517 acutely treated with either BSA or 400uM of BSA-palmitate for 4 hours in unlabelled culture
518 media, or media containing [U-$^{13}C_6$]-L-glucose or [U-$^{13}C_3$]-L-lactate.
519
520 Sample preparation for Acyl-CoA analysis
521 Acyl-CoAs were extracted by adding 100 µl of a methanol/water solution (80/20, v/v) to a cell
522 pellet spiked with 17:0-CoA (400 nM) as internal standard. Samples were thoroughly vortexed,
523 centrifuged at 1600g for 10 min at 4°C, and the supernatant transferred to a new vial for HPLC-

524 MS analysis. Solvents used for extractions and mass spectrometric analyses were of HPLC grade
525 or higher from Burdick and Jackson (Muskegon, MI).
526
527 Acyl-CoA LC-MS analysis
528 The cell extracts containing the Acyl-CoA metabolites were analyzed by reverse phase
529 chromatography using a Shimadzu HPLC (Columbia, MD) connected to an API 5000 triple
530 quadrupole mass spectrometer (AB Sciex, Framingham, MA). The samples were resolved using a
531 2 x 150 mm, 2 µm particle size C8 column (Phenomenex) with a gradient solvent system consisting
532 of solvents (A): water containing 0.1% ammonium hydroxide and (B): acetonitrile containing
533 0.1% ammonium hydroxide at a flow rate of 350 µl/min. Samples were applied to the column at
534 5% B (0.8 min) and eluted by increasing solvent B from 5% to 55% over 20 minutes and held at
535 5% for 5 min. The gradient was then returned to the starting conditions, and the column re-
536 equilibrated at 5% B for 10 min. The following settings for the mass spectrometer were used:
537 Source temperature 650 °C; ionization spray voltage 5500 V; CAD 5.0 a.u.; Curtain gas 40 a.u.;
538 GS1 55 a.u.; GS2 60 a.u.; EP 10V; CXP 12V DP 80 V CE 35V. Multiple reaction monitoring in
539 positive ion mode was performed following the neutral loss of a common CoA 507 amu fragment.
540 The mass of the endogenous Acyl-CoA species was confirmed using HPLC-coupled to a high-
541 resolution Q Exactive mass spectrometer (Thermo, San Jose, CA).
542
543 Metabolomic analysis
544 The levels of metabolites in the H9c2 cells were measured by gas chromatography–mass
545 spectrometry (GC-MS) analysis. All GC-MS analysis was performed with a Waters GCT Premier
546 mass spectrometer fitted with an Agilent 6890 gas chromatograph and a Gerstel MPS2
547 autosampler. Dried samples were suspended in 40 µL of a 40 mg/mL O-methoxylamine
548 hydrochloride (MOX) in pyridine and incubated for 1 h at 30°C. 10 µL of N-methyl-N-
549 trimethylsilyltrifluoracetamide (MSTFA) was added automatically via the autosampler and
550 incubated for 60 min at 37°C with shaking. After incubation 3 µL of a fatty acid methyl ester
551 standard solution was added via the autosampler. Then 1 µL of the prepared sample was injected
552 to the gas chromatograph inlet in the split mode with the inlet temperature held at 250°C. A 10:1
553 split ratio was used for analysis. The gas chromatograph had an initial temperature of 95°C for one
554 minute followed by a 40°C/min ramp to 110°C and a hold time of 2 min. This was followed by a

555 second 5°C/min ramp to 250°C, a third ramp to 350°C, then a final hold time of 3 min. A 30 m
556 Phenomex ZB5-5 MSi column with a 5 m long guard column was employed for chromatographic
557 separation. Helium was used as the carrier gas at 1 mL/min. Data was extracted from each
558 chromatogram as area under the curve for individual metabolites. Each sample was first
559 normalized to the added standard d4-succinate to account for extraction efficiency followed by
560 normalization to cell number. Due to this being a broad scope metabolomics analysis, no
561 normalization for ionization efficiency or concentration standards was performed.
562
563 GTEx tissue-expression and DepMap metabolite correlation
564 GTEx tissue expression data was acquired from the public GTEx portal
565 ((https://www.gtexportal.org/home/). DepMap expression data was downloaded from DepMap
566 release 21Q3 (CCLE_expression) and metabolomics data was downloaded from DepMap CCLE
567 2019 (CCLE_metabolomics_20190502) (*37, 38*). Populations of cells with high expression of
568 LDHA and LDHB ($LDHA^{Hi}$ $LDHB^{Hi}$) and high expression of LDHA and low expression of LDHB
569 ($LDHA^{Hi}$ $LDHB^{Lo}$) were determined based on z-score with $LDHA^{Hi}$ $LDHB^{Lo}$ cells defined as two
570 standard deviations below the mean. Metabolomics data were split according to LDHA LDHB
571 status and the Spearman correlation was determined for each metabolite against each other
572 metabolite. Spearman correlations were plotted according to rank and acyl-carnitines are indicated.

Fig. S1

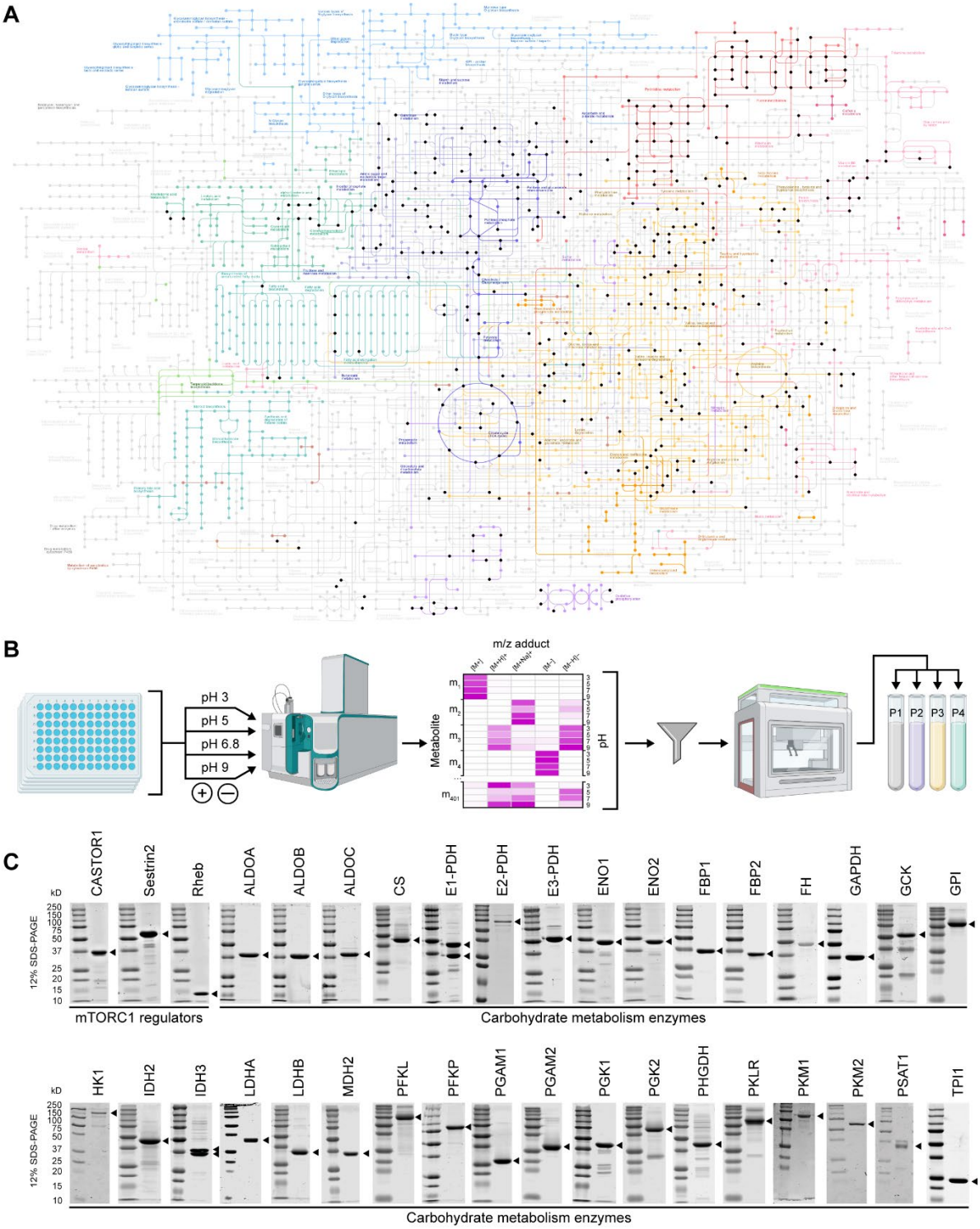
A
B
pH 3
pH 5
pH 6.8
pH 9
m/z adduct
Metabolite
pH
P1
P2
P3
P4
C
CASTOR1
Sestrin2
Rheb
ALDOA
ALDOB
ALDOC
CS
E1-PDH
E2-PDH
E3-PDH
ENO1
ENO2
FBP1
FBP2
FH
GAPDH
GCK
GPI
kD
12% SDS-PAGE
mTORC1 regulators
Carbohydrate metabolism enzymes
HK1
IDH2
IDH3
LDHA
LDHB
MDH2
PFKL
PFKP
PGAM1
PGAM2
PGK1
PGK2
PHGDH
PKLR
PKM1
PKM2
PSAT1
TPI1
Carbohydrate metabolism enzymes

574 **Figure S1. MIDAS metabolite library construction and validation and screened proteins.**
575 **(A)** The MIDAS metabolite library overlaid on KEGG human metabolic pathways
576 (https://www.genome.jp/kegg/pathway/map/map01100.html). Human pathways, colored; non-
577 human pathways, light grey. Metabolites from the MIDAS metabolite library, black spheres. **(B)**
578 FIA-MS scouting method to determine optimal MIDAS metabolite pools. Metabolites from the
579 MIDAS metabolite library were arrayed across five 96-well plates in water. Each metabolite was
580 individual analyzed at mobile phase pH 3, 5, 6.8, and 9, in positive and negative mode, by FIA-
581 MS. For each metabolite analyzed by FIA-MS ($m_1 – m_{401}$), accurate mass was verified and optimal
582 signal was determined from the extracted ion chromatogram of each metabolite adduct, mobile
583 phase pH, and polarity (increasing FIA-MS signal is colored white to magenta; Data S2. FIA-MS
584 scout). The optimal FIA-MS signal conditions for each metabolite were manually filtered and
585 binned to program an automated liquid handling method to construct the MIDAS metabolite pools
586 (P1, P2, P3, and P4) according to the specific conditions of metabolite analysis by FIA-MS. **(C)**
587 SDS-PAGE analysis of the purified target proteins analyzed by MIDAS. Target proteins are
588 annotated (arrows). E1-PDH and IDH3 samples are composed of heteromeric protein complexes.
589 mTORC1 regulators and the enzymes from carbohydrate metabolism are labeled.
590

Fig. S2

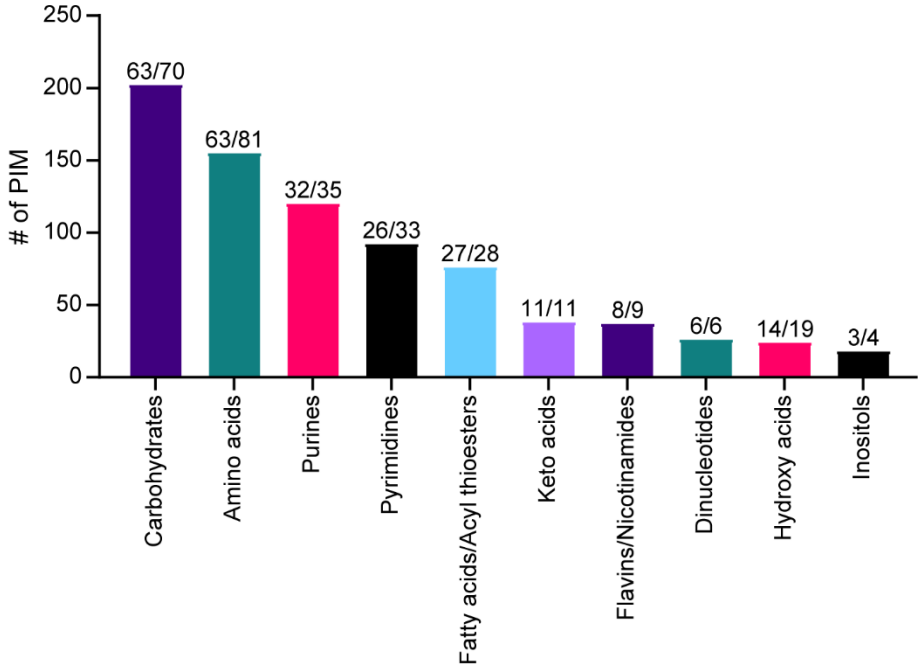
250
200
150
100
50
0
# of PIM
63/70
63/81
32/35
26/33
27/28
11/11
8/9
6/6
14/19
3/4
Carbohydrates
Amino acids
Purines
Pyrimidines
Fatty acids/Acyl thioesters
Keto acids
Flavins/Nicotinamides
Dinucleotides
Hydroxy acids
Inositols

592 **Figure S2. Metabolite sub-classes that interact with enzymes in carbohydrate metabolism.**
593 The top ten metabolite sub-classes by total PMI count across 33 enzymes in human carbohydrate
594 metabolism. The values above each column indicate the unique number of metabolites in that sub-
595 class that were identified as PMIs (numerator) and the total number metabolites in that sub-class
596 in the MIDAS metabolite library (denominator). Metabolite sub-classes were modified from
597 HMDB chemical taxonomy sub-class.

Fig. S3

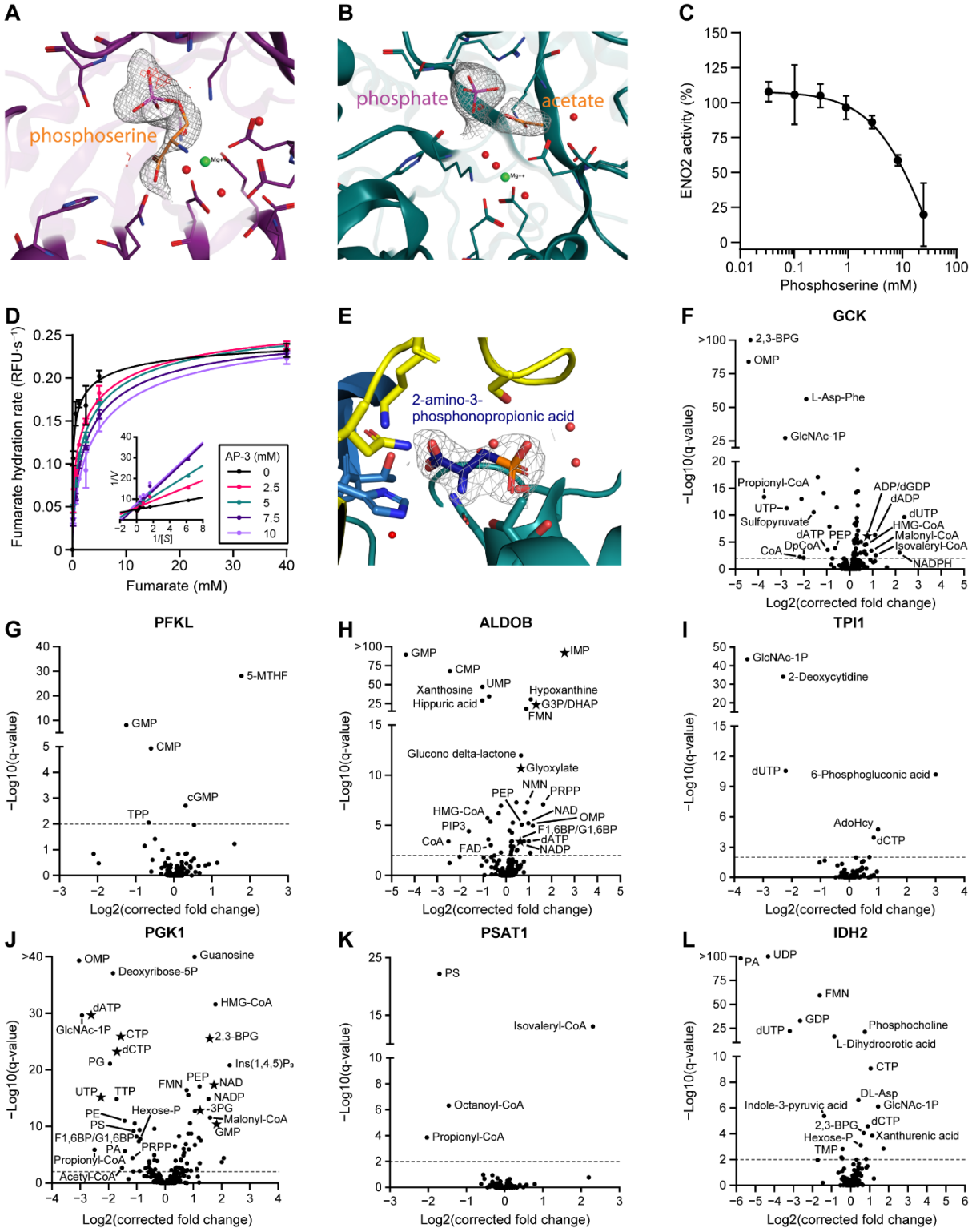
A
phosphoserine
B
phosphate
acetate
C
ENO2 activity (%)
Phosphoserine (mM)
D
Fumarate hydration rate (RFU·s⁻¹)
Fumarate (mM)
AP-3 (mM)
0
2.5
5
7.5
10
1/V
1/[S]
E
2-amino-3-phosphonopropionic acid
F
GCK
2,3-BPG
OMP
L-Asp-Phe
GlcNAc-1P
Propionyl-CoA
UTP
Sulfopyruvate
ADP/dGDP
dADP
dUTP
HMG-CoA
Malonyl-CoA
Isovaleryl-CoA
dATP
PEP
DpCoA
CoA
NADPH
−Log10(q-value)
Log2(corrected fold change)
G
PFKL
5-MTHF
GMP
CMP
cGMP
TPP
H
ALDOB
GMP
IMP
CMP
Xanthosine
UMP
Hypoxanthine
Hippuric acid
G3P/DHAP
FMN
Glucono delta-lactone
Glyoxylate
NMN
PRPP
PEP
HMG-CoA
NAD
OMP
PIP3
F1,6BP/G1,6BP
CoA
dATP
FAD
NADP
I
TPI1
GlcNAc-1P
2-Deoxycytidine
dUTP
6-Phosphogluconic acid
AdoHcy
dCTP
J
PGK1
OMP
Guanosine
Deoxyribose-5P
HMG-CoA
dATP
GlcNAc-1P
CTP
2,3-BPG
dCTP
PG
Ins(1,4,5)P₃
UTP
TTP
FMN
PEP
NAD
NADP
PE
Hexose-P
3PG
PS
Malonyl-CoA
F1,6BP/G1,6BP
GMP
PA
PRPP
Propionyl-CoA
Acetyl-CoA
K
PSAT1
PS
Isovaleryl-CoA
Octanoyl-CoA
Propionyl-CoA
L
IDH2
PA
UDP
FMN
GDP
dUTP
Phosphocholine
L-Dihydroorotic acid
CTP
DL-Asp
Indole-3-pyruvic acid
GlcNAc-1P
2,3-BPG
dCTP
Hexose-P
Xanthurenic acid
TMP

599 **Figure S3. Metabolite interactions with enolase, fumarase, and other enzymes in**
600 **carbohydrate metabolism.**
601 **(A and B)** Unbiased Fo-FcWT omit map contoured at 2.5σ for the enolase active sites depicting
602 the electron density for (A) the phosphoserine bound to the active site pocket of protomer chain B
603 and (B) the phosphate and acetate ions bound at the active site of protomer chain A. **(C)** Activity
604 of enolase determined in the presence of varying concentrations of phosphoserine. The experiment
605 was performed in triplicate and the mean ± SD are plotted. Line of best fit determined using the
606 sigmoidal, 4PL non-linear regression in GraphPad Prism 9. **(D)** Relative fumarase activity in the
607 presence of varying concentrations of substrate, fumarate, and 2-amino-3-phosphonopropionic
608 acid (AP-3). (Inset) Lineweaver–Burk plot demonstrating competitive inhibition. The experiment
609 was performed in triplicate and the mean ± SD are plotted. Lines of best fit determined using the
610 non-linear regression competitive inhibition model from GraphPad Prism 9. **(E)** Mesh
611 representation of the final 2Fo–Fc electron density map contoured at 1.0 σ level (gray) for 2-amino-
612 3-phosphonoproprionic acid (blue) in the human fumarase active site. **(F – L)** Volcano plots of
613 MIDAS metabolite interaction with glucokinase (GCK), liver 6-phosphofructokinase (PFKL),
614 aldolase B (ALDOB), triosephosphate isomerase (TPI1), phosphoglycerate kinase 1 (PGK1),
615 phosphoserine aminotransferase 1 (PSAT1), and NADP-dependent isocitrate dehydrogenase 2
616 (IDH2). Stars indicate a previously known human PMI primarily sourced from BRENDA
617 (https://www.brenda-enzymes.org/index.php). MIDAS analysis of all proteins was performed by
618 triplicate equilibrium dialysis and technical triplicate FIA-MS injections. Specific, significant
619 PMIs identified by MIDAS are labeled and have a q-value < 0.01 (dotted line).

Fig. S4

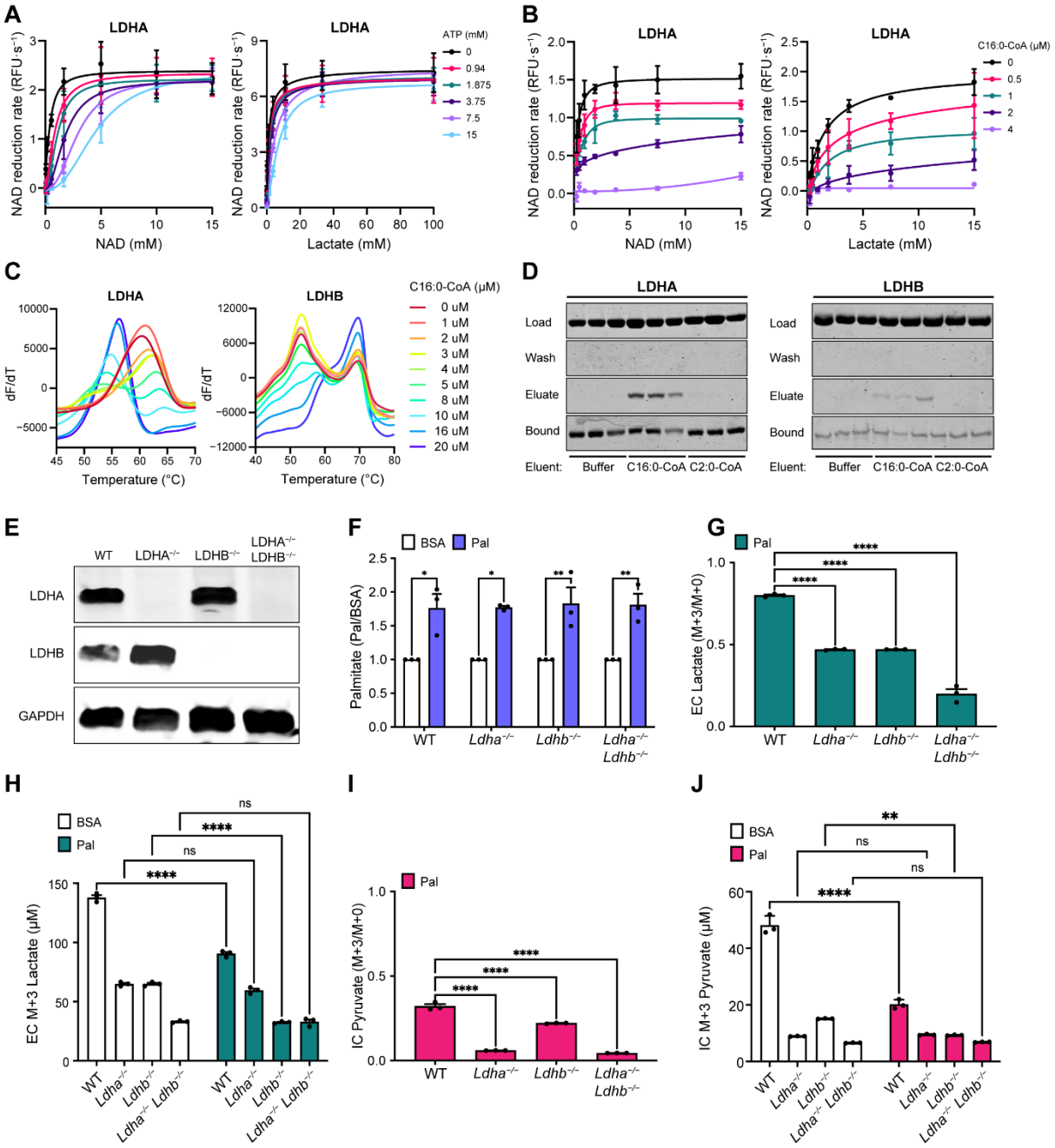
A
LDHA
NAD reduction rate (RFU·s⁻¹)
NAD (mM)
Lactate (mM)
ATP (mM)
0
0.94
1.875
3.75
7.5
15
B
LDHA
NAD reduction rate (RFU·s⁻¹)
NAD (mM)
Lactate (mM)
C16:0-CoA (μM)
0
0.5
1
2
4
C
LDHA
LDHB
dF/dT
Temperature (°C)
C16:0-CoA (μM)
0 uM
1 uM
2 uM
3 uM
4 uM
5 uM
8 uM
10 uM
16 uM
20 uM
D
LDHA
LDHB
Load
Wash
Eluate
Bound
Eluent:
Buffer
C16:0-CoA
C2:0-CoA
E
WT
LDHA⁻/⁻
LDHB⁻/⁻
LDHA⁻/⁻ LDHB⁻/⁻
LDHA
LDHB
GAPDH
F
BSA
Pal
Palmitate (Pal/BSA)
WT
Ldha⁻/⁻
Ldhb⁻/⁻
Ldha⁻/⁻ Ldhb⁻/⁻
G
Pal
EC Lactate (M+3/M+0)
H
BSA
Pal
EC M+3 Lactate (μM)
ns
I
Pal
IC Pyruvate (M+3/M+0)
J
BSA
Pal
IC M+3 Pyruvate (μM)

621 **Figure S4. Lactate dehydrogenase interacts with and is inhibited by nucleotides and long-**
622 **chain acyl-CoA.**
623 **(A)** Relative LDHA activity was determined in the presence of varying concentrations of substrate,
624 NAD or lactate, and ATP. Experiments were performed in triplicate and the mean ± SD are plotted.
625 Non-linear regression competitive inhibition modeling were fit using GraphPad Prism 9 software.
626 **(B)** Relative LDHA activity was determined in the presence of varying concentrations of substrate,
627 NAD or lactate, and palmitoyl-CoA (C16:0-CoA). Experiments were performed in triplicate and
628 the mean ± SD are plotted. Non-linear regression non-competitive inhibition modeling were fit
629 using GraphPad Prism 9 software. **(C)** LDHA and LDHB were analyzed by PROTEOSTAT DSF
630 in the presence of increasing concentrations of C16:0-CoA. dF/dT was determined as a function
631 of temperature. Representative experiments from triplicate experiments each with sextuplicate
632 technical replicates are presented. **(D)** Palmitoyl-CoA-Agarose pull-down assay with LDHA or
633 LDHB treated with buffer control, C16:0-CoA, or acetyl-CoA (C2:0-CoA) (Eluent). Protein input
634 (Load), post-5x wash (Wash), concentrated supernatant post-eluent treatment (Eluate), protein
635 bound to palmitoyl-CoA-agarose beads post-eluent treatment (Bound). The experiment was
636 performed in technical triplicate. **(E)** Representative immunoblot of LDHA and LDHB in the
637 indicated H9c2-derived cell lines. **(F)** Fold change of intracellular palmitate in *Ldha*$^{-/-}$, *Ldhb*$^{-/-}$,
638 or *Ldha*$^{-/-}$ *Ldhb*$^{-/-}$ H9c2 cell lines in response to treatment with palmitate-conjugated BSA (Pal)
639 relative to BSA-vehicle control (BSA). **(G)** Changes in ^{13}C enrichment of extracellular lactate in
640 *Ldha*$^{-/-}$, *Ldhb*$^{-/-}$, or *Ldha*$^{-/-}$ *Ldhb*$^{-/-}$ H9c2 cell lines in response to treatment with palmitate-
641 conjugated BSA. **(H)** Concentration of ^{13}C-labelled extracellular lactate in *Ldha*$^{-/-}$, *Ldhb*$^{-/-}$, or
642 *Ldha*$^{-/-}$;*Ldhb*$^{-/-}$ H9c2 cell lines in response to BSA-vehicle control (BSA) or palmitate-
643 conjugated BSA (Pal) treatment. **(I)** Changes in intracellular ^{13}C enrichment of pyruvate in
644 *Ldha*$^{-/-}$, *Ldhb*$^{-/-}$, or *Ldha*$^{-/-}$ *Ldhb*$^{-/-}$ H9c2 cell lines in response to treatment with palmitate-
645 conjugated BSA. **(J)** Concentration of intracellular ^{13}C-labelled pyruvate in *Ldha*$^{-/-}$, *Ldhb*$^{-/-}$, or
646 *Ldha*$^{-/-}$ *Ldhb*$^{-/-}$ H9c2 cell lines in response to BSA vehicle control (BSA) or palmitate-conjugated
647 BSA (Pal) treatment. **(F – J)** All experiments were performed in triplicate. Data are presented as
648 mean ± SD. $*p < 0.05$, $**p < 0.01$, $***p < 0.001$, $****p < 0.0001$, determined by one-way
649 ANOVA and Sidak's multiple comparison test.

Fig. S5

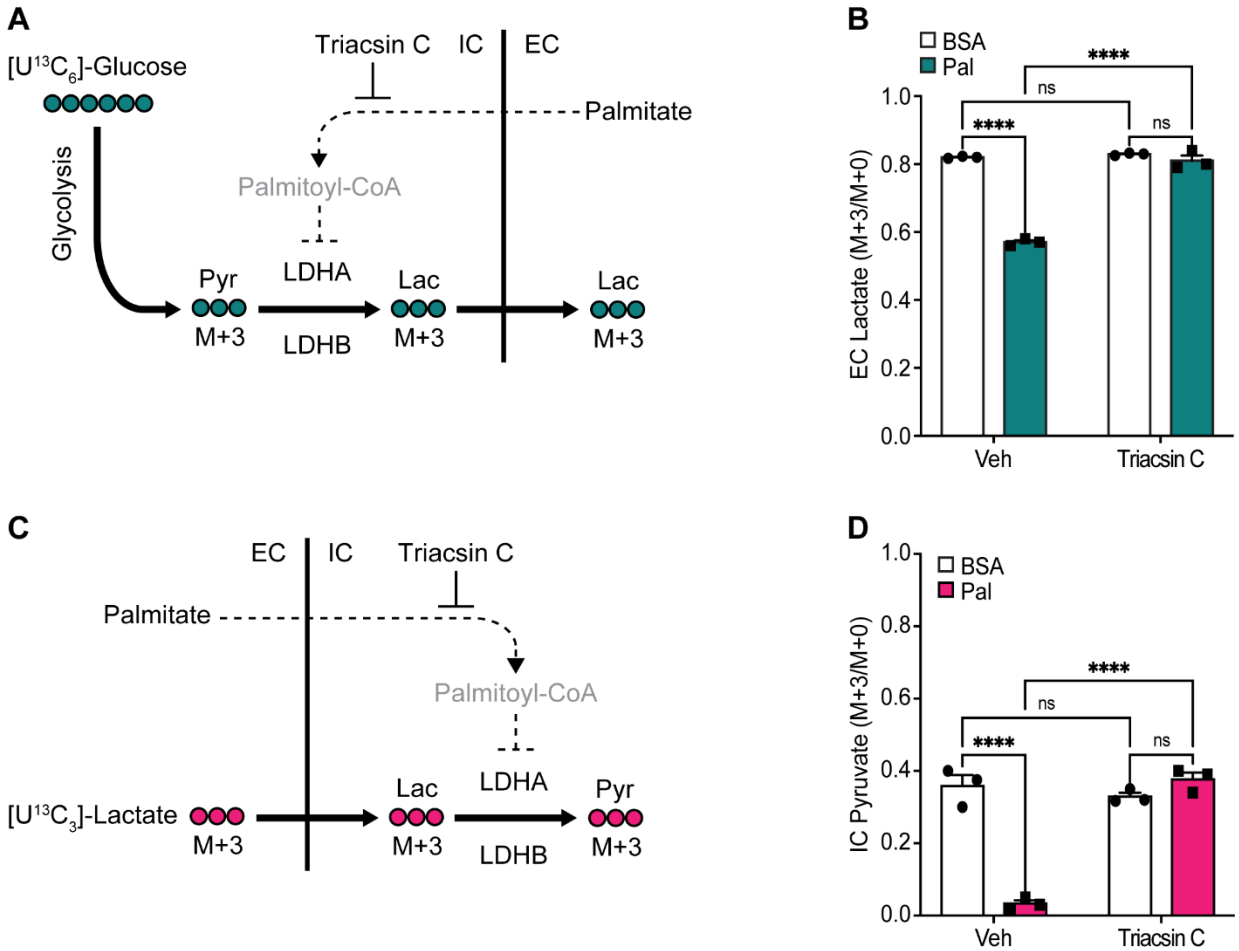
A
[U13C6]-Glucose
Glycolysis
Triacsin C
IC
EC
Palmitate
Palmitoyl-CoA
LDHA
Pyr
M+3
LDHB
Lac
M+3
Lac
M+3
B
BSA
Pal
EC Lactate (M+3/M+0)
1.0
0.8
0.6
0.4
0.2
0.0
****
ns
****
ns
Veh
Triacsin C
C
EC
IC
Triacsin C
Palmitate
Palmitoyl-CoA
LDHA
[U13C3]-Lactate
M+3
Lac
M+3
LDHB
Pyr
M+3
D
BSA
Pal
IC Pyruvate (M+3/M+0)
1.0
0.8
0.6
0.4
0.2
0.0
****
ns
****
ns
Veh
Triacsin C

651 **Figure S5. Inhibiton of acyl-CoA synthease prevents inhibition of LDHA by palmitate.**
652 **(A)** Schematic of [$U^{13}C_6$]-glucose metabolism in cells treated with acyl-CoA synthase inhibitor,
653 triacsin C, and palmitate-conjugated BSA following inhibition of the mitochondrial pyruvate
654 carrier with UK5099. Pyruvate, Pyr; lactate, Lac; IC, intracellular; EC, extracellular. **(B)** Changes
655 in ^{13}C enrichment of extracellular lactate in H9c2 cell lines in response to treatment with palmitate-
656 conjugated BSA and triacsin C. Vehicle (Veh) indicates no triacsin C treatment. **(C)** Schematic of
657 [$U^{13}C_3$]-lactate metabolism in cells treated with acyl-CoA synthase inhibitor, triacsin C, and
658 palmitate-conjugated BSA (Pal) following inhibition of the mitochondrial pyruvate carrier with
659 UK5099. Pyruvate, Pyr; lactate, Lac; IC, intracellular; EC, extracellular. **(D)** Changes in ^{13}C
660 enrichment of intracellular pyruvate in H9c2 cell lines in response to treatment with palmitate-
661 conjugated BSA (Pal) and triacsin C. Vehicle (Veh) indicates no triacsin C treatment. **(B and D)**
662 Experiments were performed in triplicate and mean ± SD are displayed. One-way ANOVA and
663 Sidak's multiple comparison test was performed between Pal and BSA samples with and without
664 triacsin C ($p < 0.0001$, ****; non-significant, ns).

Fig. S6

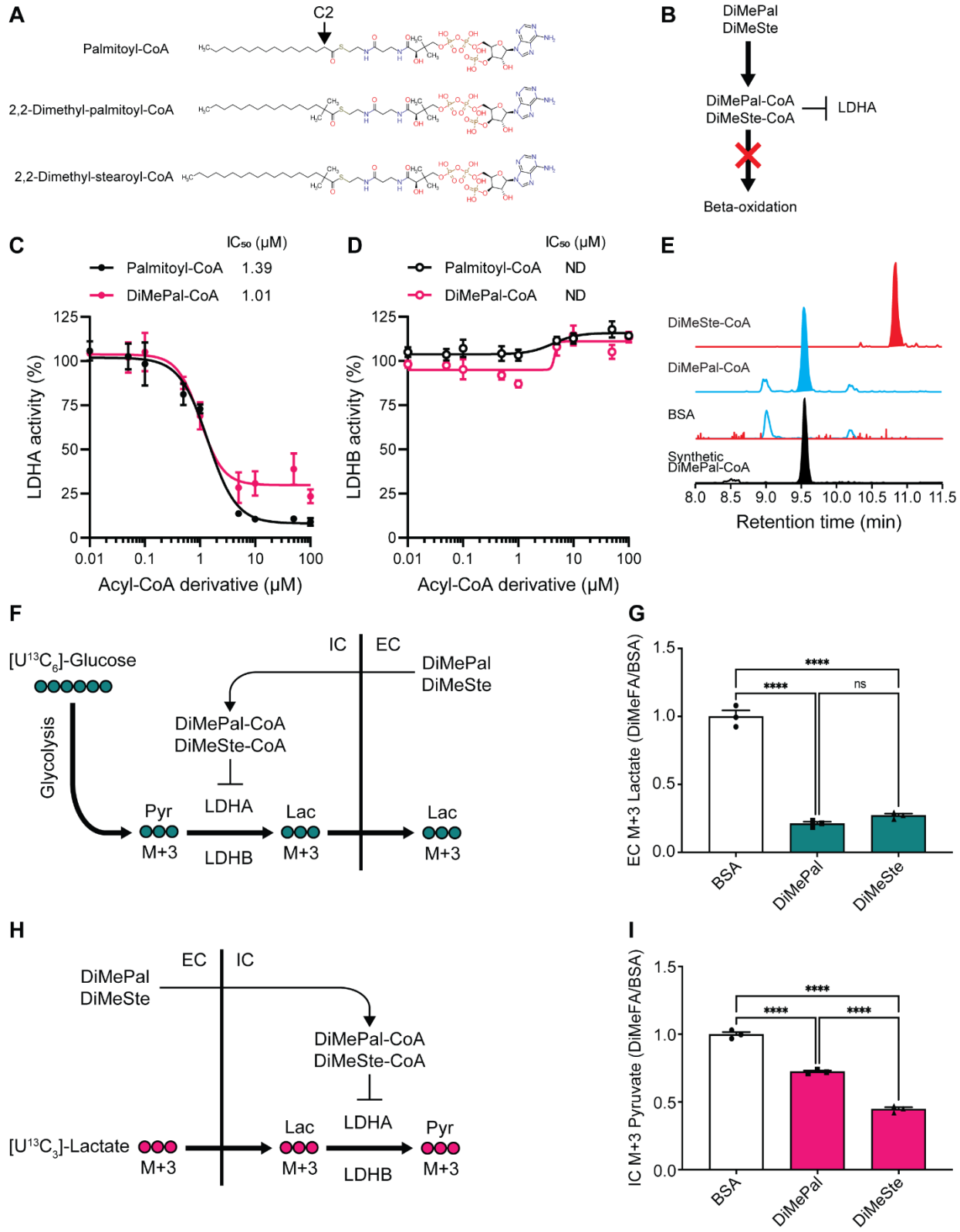
A
C2
Palmitoyl-CoA
2,2-Dimethyl-palmitoyl-CoA
2,2-Dimethyl-stearoyl-CoA
B
DiMePal
DiMeSte
DiMePal-CoA
DiMeSte-CoA
LDHA
Beta-oxidation
C
IC50 (μM)
Palmitoyl-CoA 1.39
DiMePal-CoA 1.01
LDHA activity (%)
Acyl-CoA derivative (μM)
D
IC50 (μM)
Palmitoyl-CoA ND
DiMePal-CoA ND
LDHB activity (%)
Acyl-CoA derivative (μM)
E
DiMeSte-CoA
DiMePal-CoA
BSA
Synthetic DiMePal-CoA
Retention time (min)
F
[U13C6]-Glucose
Glycolysis
IC
EC
DiMePal
DiMeSte
DiMePal-CoA
DiMeSte-CoA
LDHA
Pyr
M+3
LDHB
Lac
M+3
Lac
M+3
G
EC M+3 Lactate (DiMeFA/BSA)
****
****
ns
BSA
DiMePal
DiMeSte
H
EC
IC
DiMePal
DiMeSte
DiMePal-CoA
DiMeSte-CoA
LDHA
[U13C3]-Lactate
M+3
Lac
M+3
LDHB
Pyr
M+3
I
IC M+3 Pyruvate (DiMeFA/BSA)
****
****
****
BSA
DiMePal
DiMeSte

666 **Figure S6. LDHA is inhibited by non-oxidizable long-chain acyl-CoA analogs.**
667 **(A)** Palmitoyl-CoA and the non-oxidizable, long-chain acyl-CoA analogs, 2,2-dimethyl-
668 palmitoyl-CoA (DiMePal-CoA) and 2,2-dimethyl-strearoyl-CoA (DiMeSte-CoA). Dimethylated
669 C2 carbon position indicated (C2 arrow). **(B)** Schematic of dimethyl-palmitate (DiMePal) and
670 dimethyl-strearate (DiMeSte) metabolism. DiMePal and DiMeSte are esterified to CoA by
671 intracellular acyl-CoA synthase to generate DiMePal-CoA and DiMeSte-CoA. DiMePal-CoA and
672 DiMeSte-CoA inhibit LDHA and cannot be utilized as substrates in fatty acid beta-oxidation. **(C**
673 **and D)** Enzyme activity of LDHA (filled circles) or LDHB (open circles) treated with palmitoyl-
674 CoA (black) or DiMePal-CoA (pink). Half maximal inhibitory concentration (IC_{50}) was
675 determined from triplicate experiments each with technical triplicates using GraphPad Prism 9;
676 ND, not determined. Mean ± SD is displayed from triplicate experiments. **(E)** LC-MS/MS shows
677 the endogenous formation of DiMeSte-CoA and DiMePal-CoA in H9c2 cells treated with
678 DiMeSte-conjugated BSA or DiMePal-conjugated BSA, respectively. No peaks were detected in
679 BSA treated cells. Endogenous DiMePal-CoA co-eluted with synthetic DiMePal-CoA used in (C
680 and D). **(F)** Schematic of [$U^{13}C_6$]-glucose metabolism in cells treated with DiMePal or DiMeSte
681 following inhibition of the mitochondrial pyruvate carrier with UK5099. Pyruvate, Pyr; lactate,
682 Lac; IC, intracellular; EC, extracellular. **(G)** Fold change of extracellular [$U^{13}C_3$]-lactate from
683 H9c2 cells in response to treatment with DiMePal- or DiMeSte-conjugated BSA relative to BSA-
684 vehicle control. **(H)** Schematic of [$U^{13}C_3$]-lactate metabolism in cells treated with DiMePal or
685 DiMeSte following inhibition of the mitochondrial pyruvate carrier with UK5099. Pyruvate, Pyr;
686 lactate, Lac; IC, intracellular; EC, extracellular. **(I)** Fold change of intracellular [$U^{13}C_3$]-pyruvate
687 from H9c2 cells in response to treatment with DiMePal- or DiMeSte-conjugated BSA relative to
688 BSA-vehicle control. **(G and I)** Experiments were performed in triplicate and mean ± SD are
689 displayed. One-way ANOVA and Sidak's multiple comparison test was performed between
690 DiMePal-, DiMeSte-, and BSA-treated samples ($p < 0.0001$, ****; non-significant, ns).
691

Fig. S7

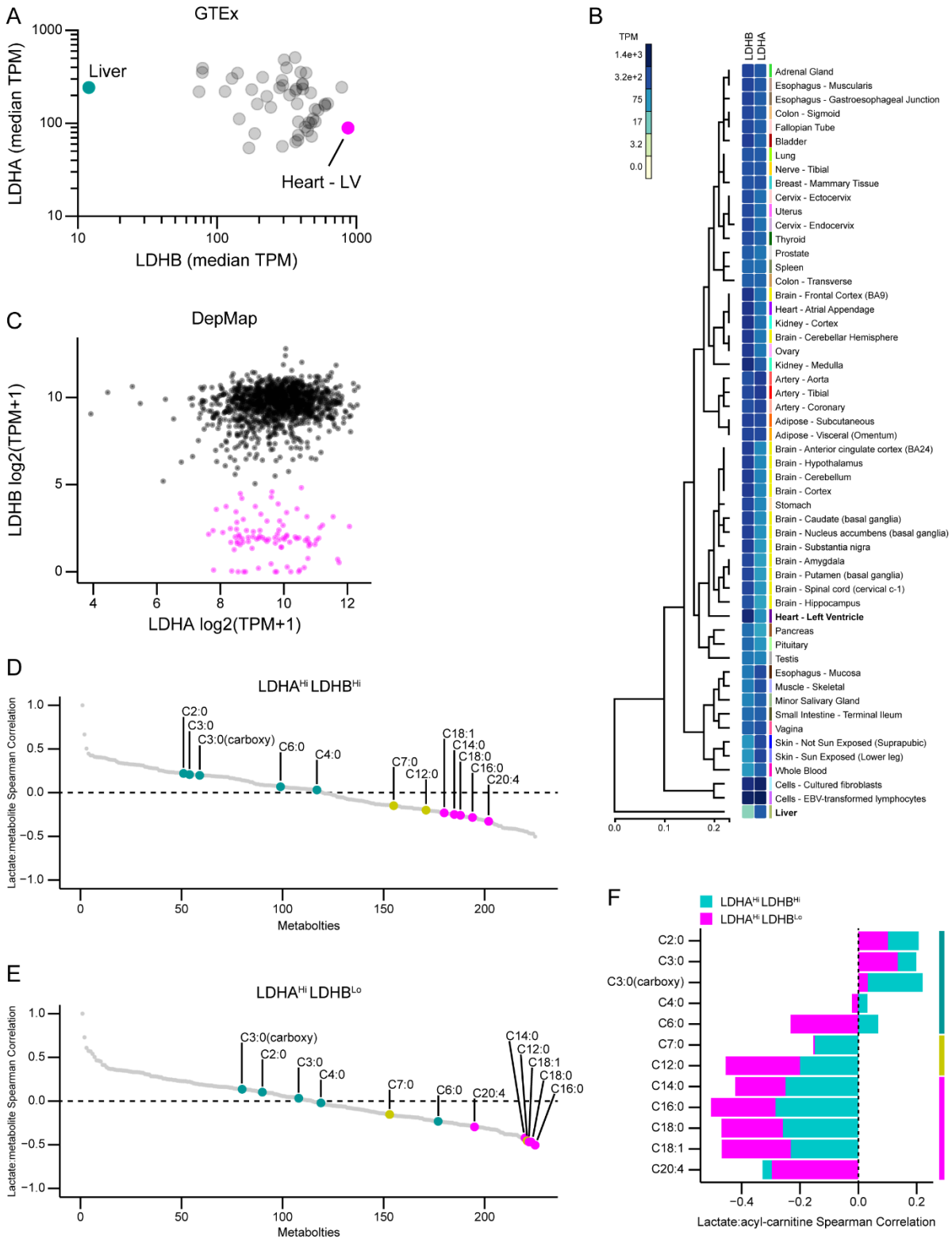
A
GTEx
LDHA (median TPM)
LDHB (median TPM)
Liver
Heart - LV
B
TPM
LDHB
LDHA
Adrenal Gland
Esophagus - Muscularis
Esophagus - Gastroesophageal Junction
Colon - Sigmoid
Fallopian Tube
Bladder
Lung
Nerve - Tibial
Breast - Mammary Tissue
Cervix - Ectocervix
Uterus
Cervix - Endocervix
Thyroid
Prostate
Spleen
Colon - Transverse
Brain - Frontal Cortex (BA9)
Heart - Atrial Appendage
Kidney - Cortex
Brain - Cerebellar Hemisphere
Ovary
Kidney - Medulla
Artery - Aorta
Artery - Tibial
Artery - Coronary
Adipose - Subcutaneous
Adipose - Visceral (Omentum)
Brain - Anterior cingulate cortex (BA24)
Brain - Hypothalamus
Brain - Cerebellum
Brain - Cortex
Stomach
Brain - Caudate (basal ganglia)
Brain - Nucleus accumbens (basal ganglia)
Brain - Substantia nigra
Brain - Amygdala
Brain - Putamen (basal ganglia)
Brain - Spinal cord (cervical c-1)
Brain - Hippocampus
Heart - Left Ventricle
Pancreas
Pituitary
Testis
Esophagus - Mucosa
Muscle - Skeletal
Minor Salivary Gland
Small Intestine - Terminal Ileum
Vagina
Skin - Not Sun Exposed (Suprapubic)
Skin - Sun Exposed (Lower leg)
Whole Blood
Cells - Cultured fibroblasts
Cells - EBV-transformed lymphocytes
Liver
C
DepMap
LDHB log2(TPM+1)
LDHA log2(TPM+1)
D
LDHA^Hi LDHB^Hi
Lactate:metabolite Spearman Correlation
Metabolties
E
LDHA^Hi LDHB^Lo
Lactate:metabolite Spearman Correlation
Metabolties
F
LDHA^Hi LDHB^Hi
LDHA^Hi LDHB^Lo
Lactate:acyl-carnitine Spearman Correlation

693 **Figure S7. LDH tissue expression differences correlate with the lactate:acyl-carnitine ratio.**
694 **(A)** Scatter plot depicting median transcripts per million (TPM) for LDHA and LDHB across
695 human tissues. **(B)** Heatmap depicting median TPM for LDHA and LDHB across human tissues.
696 **(A and B)** Data obtained through GTEx Portal (https://www.gtexportal.org/home/). **(C)** LDHA
697 and LDHB expression (TPM) across the 928 cancer cell lines from DepMap (*37, 38*). Cells
698 expressing high LDHA and LDHB ($LDHA^{Hi}$ $LDHB^{Hi}$), black; cells expressing high LDHA and
699 low LDHB ($LDHA^{Hi}$ $LDHB^{Lo}$), magenta. **(D)** Spearman correlation of lactate to all measured
700 metabolites from DepMap for $LDHA^{Hi}$ $LDHB^{Hi}$ cells. **(E)** Spearman correlation of lactate to all
701 measured metabolites from DepMap for $LDHA^{Hi}$ $LDHB^{Lo}$ cells. **(D and E)** short- (teal), medium-
702 (yellow), and long-chain (magenta) acyl-carinitines are labeled according to their acyl chain
703 composition. **(F)** Overlapped spearman correlations of lactate:acyl-carnitines for $LDHA^{Hi}$ $LDHB^{Hi}$
704 and $LDHA^{Hi}$ $LDHB^{Lo}$ cells from (D) and (E). (Right) Short- (teal), medium- (yellow), and long-
705 chain (magenta) acyl-carinitines are indicated adjacent.

706 **Table S1. Metabolite abbreviations.**

Metabolite abbreviation	Metabolite name
1,3-BPG	1,3-bisphosphoglycerate
2,3-BPG	2,3-Diphospho-D-glyceric acid
2PG	2-phosphoglycerate
3,5-Diiodo-L-Tyr	3,5-Diiodo-L-Tyrosine
3PG	D-3-Phosphoglyceric acid
3-PHP	Phosphohydroxypyruvic acid
5-MTHF	5-methyltetrahydrofolic acid
AdoHcy	S-(5-Adenosyl)-L-homocysteine
ADP	Adenosine diphosphate
AMP	Adenosine monophosphate
AP-3	DL-2-Amino-3-phosphonopropionic acid
AP3A	Diadenosine triphosphate
ATP	Adenosine triphosphate
C12:0-CoA	Lauroyl coenzyme A
C16:0-CoA	Palmitoyl coenzyme A
C18:1-CoA	Oleoyl coenzyme A
C2:0-CoA	Acetyl coenzyme A
C20:0-CoA	Arachidonoyl coenzyme A
C4:0-CoA	Butryl coenzyme A
C8:0-CoA	Octanoyl coenzyme A
cAMP	cyclic adenosine monophosphate
CDP	Cytidine 5-diphosphate
cGMP	cyclic guanosine monophosphate
Cit	Citrate
CMP	Cytidine monophosphate
CoA	Coenzyme A
CTP	Cytidine 5-triphosphate
dADP	Deoxyadenosine diphosphate
dAMP	Deoxyadenosine monohosphate
dATP	2-Deoxyadenosine 5-triphosphate
dCMP	2-Deoxy-5-cytidylic acid
dCTP	Deoxycytidine triphosphate
Deoxyribose-5P	2-Deoxyribose-5-phosphate
dGDP	2-Deoxyguanosine 5-diphosphate
dGMP	Deoxyguanylate
DHAP	Dihydroxyacetone phosphate, Glycerone phosphate
DiMePal	2,2-Dimethyl-palmitate
DiMeSte	2,2-Dimethyl-stearate
DiMePal-CoA	2,2-Dimethyl-palmitoyl coenzyme A
DiMeSte-CoA	2,2-Dimethyl-stearoyl coenzyme A

DL-Asp	DL-Aspartate
DpCoA	Dephosphocoenzyme A
dUTP	Deoxyuridine triphosphate
F1,6BP	D-Fructose 1,6-bisphosphate
F6P	D-Fructose 6-phosphate
FAD	Flavin adenine dinucleotide
FMN	Riboflavin 5-monophosphate
Fum	Fumarate
G1,6BP	D-Glucose 1,6-bisphosphate
G3P	D-Glyceraldehyde 3-phosphate
G6P	D-Glucose 6-phosphate
GDP	Guanosine 5-diphosphate
GlcN-6P	D-Glucosamine 6-phosphate
GlcNAc-1P	N-Acetyl-D-glucosamine 1-phosphate
GlcNAc-6P	N-Acetyl-D-glucosamine 6-phosphate
Glycerol-3P	D-Glycerol 1-phosphate
GMP	Guanosine 5-monophosphate
GTP	Guanosine 5-triphosphate
Hexose-P	D-Fructose 6-phosphate, D-Galactose 1-phosphate, D-Glucose 1-phosphate, D-Glucose 6-phosphate, D-Mannose 1-phosphate, D-Mannose 6-phosphate
HMG-CoA	3-Hydroxy-3-methylglutaryl coenzyme A
IMP	Inosine 5-monophosphate
Ins(1,4,5)P3	D-myo-Inositol-1,4,5-triphosphate
L-5-HTP	5-Hydroxy-L-tryptophan
Lac	L-Lactic acid
L-Allo-Ile	L-Alloisoleucine
L-Asp-Phe	L-a-Aspartyl-L-phenylalanine
L-Ile	L-Isoleucine
L-Leu	L-Leucine
NAD	Nicotinamide adenine dinucleotide
NADH	Nicotinamide adenine dinucleotide, reduced
NADP	nicotinamide adenine dinucleotide phosphate
NHD	Nicotinamide hypoxanthine dinucleotide
NMN	Nicotinamide ribotide
OMP	Orotidine 5-monophosphate
PA	Phosphatidic Acid
PAP	Adenosine 3,5-diphosphate
PAPS	3-Phosphoadenosine 5-phosphosulfate
P-Creatine	Phosphocreatine
PE	Phosphatidylethanolamine
Pentose-P	D-Ribose 1-phosphate, D-Ribose 5-phosphate, D-Xylulose 5-phosphate
PEP	Phosphoenolpyruvic acid
PG	Phosphatidylglycerol

Phe	L-Phenylalanine
PIP2	Phosphatidylinositol-4,5-bisphosphate C-6
PIP3	Phosphatidylinositol-3,4,5-triphosphate C-6
PRPP	5-Phospho-D-ribose 1-diphosphate
PS	Phosphatidylserine
pSer	O-Phospho-L-serine, Phosphoserine
pTyr	O-Phosphotyrosine, Phosphotyrosine
Pyr	Pyruvate
Sedo-7P	D-Sedoheptulose 7-phosphate
Ser	L-Serine
Succ-AMP	Adenylosuccinic acid
Tag-6P	D-Tagatose 6-phosphate
Thr	L-Threonine
TMP	Thymidine monophosphate
TPP	Thiamine pyrophosphate
Trp	L-Tryptophan
TTP	Thymidine 5-triphosphate
UDP	Uridine 5-diphosphate
UMP	Uridine monophosphate
UTP	Uridine 5-triphosphate
Val	L-Valine
XMP	Xanthosine 5-monophosphate

707

708 **Table S2. Phosphoserine-ENO2 data collection and refinement statistics.**

Wavelength (Å)	1.00000
Resolution range (Å)	39.89 - 2.10 (2.175 - 2.10)*
Space group	P 2_1 2_1 2_1
Unit cell (Å)	68.05 108.38 117.93
(°)	90, 90, 90
Total reflections	2,203,993 (188,723)*
Unique reflections	50,504 (4,644)*
Multiplicity	43.6 (38.5)*
Completeness (%)	96.58 (90.06)*
Mean I/sigma(I)	20.52 (1.92)*
Wilson B-factor(Å^2)	26
R-merge	0.91 (3.46)*
R-meas	0.92 (3.51)*
R-pim	0.14 (0.56)*
CC1/2	0.931 (0.539)*
CC*	0.982 (0.837)*
Reflections used in refinement	49,880 (4,573)*
Reflections used for R-free	2,482 (226)*
R-work	0.180 (0.271)*
R-free	0.235 (0.326)*
CC(work)	0.849 (0.706)*
CC(free)	0.841 (0.649)*
Number of non-hydrogen atoms	7008
macromolecules	6666
phosphate	5
magnesium	2
acetate	4
ethylene glycol	12
polyethylene glycol	10
phosphoserine	11
solvent	298
Protein residues	870
RMS(bonds)(Å)	0.007
RMS(angles)(°)	0.88
Ramachandran favored (%)	96.88
Ramachandran allowed (%)	2.89
Ramachandran outliers (%)	0.23
Rotamer outliers (%)	1.85
Clashscore	4.72
Average B-factor(Å^2)	30
macromolecules	30
phosphate	35
magnesium	27
acetate	39

ethylene glycol	46
polyethylene glycol	46
phosphoserine	47
solvent	33

*Statistics for the highest-resolution shell are shown in parentheses.

710 **Table S3. AP-3-fumarase data collection and refinement statistics.**

Wavelength (Å)	1.323630
Resolution range (Å)	49.80 - 2.15 (2.20 - 2.15)*
Space group	P 6_5 2 2
Unit cell (Å)	190.90, 190.90, 116.24
(°)	90, 90, 120
Total reflections	2,660,677 (178,767)*
Unique reflections	67,921 (4,478)*
Multiplicity	39.2 (39.9)*
Completeness (%)	100 (100)*
Mean I/sigma(I)	15.0 (1.1)*
Wilson B-factor	43
R-merge	0.25 (4.82)*
R-meas	0.26 (4.95)*
R-pim	0.06 (1.09)*
CC1/2	0.999 (0.458)*
CC*	-
Reflections used in refinement	67,877
Reflections used for R-free	3,399
R-work	0.186(0.310)*
R-free	0.209(0.330)*
CC(work)	0.965(0.641)*
CC(free)	0.955(0.675)*
Number of non-hydrogen atoms	7191
macromolecules	6847
ligands	44
solvent	300
Protein residues	922
RMS deviations (bonds)	0.0031
RMS deviations (angles)	1.266
Ramachandran favored (%)	96.82
Ramachandran allowed (%)	3.18
Ramachandran outliers (%)	0.00
Rotamer outliers (%)	0.84
Clashscore	2.92
Average B-factor	52
macromolecules	52
2-amino-3-phosphonopropionic acid	52
glycerol	56
solvent	51

711 *Statistics for the highest-resolution shell are shown in parentheses.
712

713 **Data S1. MIDAS metabolite library**

714 **Data S2. FIA-MS properties of MIDAS metabolites**

715 **Data S3. MIDAS proteins**

716 **Data S4. MIDAS protein-metabolite interactions**

717 **Supplemental references**

718 1. M. Kanehisa, S. Goto, KEGG: kyoto encyclopedia of genes and genomes. *Nucleic Acids*
719 *Res* **28**, 27-30 (2000).
720 2. D. S. Wishart *et al.*, HMDB 4.0: the human metabolome database for 2018. *Nucleic Acids*
721 *Res* **46**, D608-D617 (2018).
722 3. T. Fuhrer, D. Heer, B. Begemann, N. Zamboni, High-throughput, accurate mass
723 metabolome profiling of cellular extracts by flow injection-time-of-flight mass
724 spectrometry. *Anal Chem* **83**, 7074-7080 (2011).
725 4. D. Holbrook-Smith, S. Durot, U. Sauer, High-throughput metabolomics predicts drug-
726 target relationships for eukaryotic proteins. *Mol Syst Biol* **18**, e10767 (2022).
727 5. M. Anglada-Girotto *et al.*, Combining CRISPRi and metabolomics for functional
728 annotation of compound libraries. *Nat Chem Biol* **18**, 482-491 (2022).
729 6. J. T. Leek, J. D. Storey, Capturing heterogeneity in gene expression studies by surrogate
730 variable analysis. *PLoS Genet* **3**, 1724-1735 (2007).
731 7. A. E. Jaffe *et al.*, qSVA framework for RNA quality correction in differential expression
732 analysis. *Proc Natl Acad Sci U S A* **114**, 7130-7135 (2017).
733 8. J. D. Storey, R. Tibshirani, Statistical significance for genomewide studies. *Proc Natl Acad*
734 *Sci U S A* **100**, 9440-9445 (2003).
735 9. A. Chang *et al.*, BRENDA, the ELIXIR core data resource in 2021: new developments and
736 updates. *Nucleic Acids Res* **49**, D498-D508 (2021).
737 10. J. Chambers *et al.*, UniChem: a unified chemical structure cross-referencing and identifier
738 tracking system. *J Cheminform* **5**, 3 (2013).
739 11. E. Brunk *et al.*, Recon3D enables a three-dimensional view of gene variation in human
740 metabolism. *Nat Biotechnol* **36**, 272-281 (2018).
741 12. G. Joshi-Tope *et al.*, Reactome: a knowledgebase of biological pathways. *Nucleic Acids*
742 *Res* **33**, D428-432 (2005).
743 13. B. Jassal *et al.*, The reactome pathway knowledgebase. *Nucleic Acids Res* **48**, D498-D503
744 (2020).
745 14. A. Fabregat *et al.*, The Reactome Pathway Knowledgebase. *Nucleic Acids Res* **46**, D649-
746 D655 (2018).

747 15. J. A. Berg *et al.*, Network-aware reaction pattern recognition reveals regulatory signatures
748 of mitochondrial dysfunction. *bioRxiv*, 2020.2006.2025.171850 (2021).
749 16. F. H. Niesen, H. Berglund, M. Vedadi, The use of differential scanning fluorimetry to
750 detect ligand interactions that promote protein stability. *Nat Protoc* **2**, 2212-2221 (2007).
751 17. N. Satani *et al.*, ENOblock Does Not Inhibit the Activity of the Glycolytic Enzyme
752 Enolase. *PLoS One* **11**, e0168739 (2016).
753 18. T. G. Battye, L. Kontogiannis, O. Johnson, H. R. Powell, A. G. Leslie, iMOSFLM: a new
754 graphical interface for diffraction-image processing with MOSFLM. *Acta Crystallogr D*
755 *Biol Crystallogr* **67**, 271-281 (2011).
756 19. P. Evans, Scaling and assessment of data quality. *Acta Crystallogr D Biol Crystallogr* **62**,
757 72-82 (2006).
758 20. P. R. Evans, G. N. Murshudov, How good are my data and what is the resolution? *Acta*
759 *Crystallogr D Biol Crystallogr* **69**, 1204-1214 (2013).
760 21. A. J. McCoy *et al.*, Phaser crystallographic software. *J Appl Crystallogr* **40**, 658-674
761 (2007).
762 22. D. Liebschner *et al.*, Macromolecular structure determination using X-rays, neutrons and
763 electrons: recent developments in Phenix. *Acta Crystallogr D Struct Biol* **75**, 861-877
764 (2019).
765 23. P. Emsley, B. Lohkamp, W. G. Scott, K. Cowtan, Features and development of Coot. *Acta*
766 *Crystallogr D Biol Crystallogr* **66**, 486-501 (2010).
767 24. M. A. Ajalla Aleixo, V. L. Rangel, J. K. Rustiguel, R. A. P. de Padua, M. C. Nonato,
768 Structural, biochemical and biophysical characterization of recombinant human fumarate
769 hydratase. *FEBS J* **286**, 1925-1940 (2019).
770 25. W. Kabsch, Xds. *Acta Crystallogr D Biol Crystallogr* **66**, 125-132 (2010).
771 26. A. Vagin, A. Teplyakov, Molecular replacement with MOLREP. *Acta Crystallogr D Biol*
772 *Crystallogr* **66**, 22-25 (2010).
773 27. G. N. Murshudov, A. A. Vagin, E. J. Dodson, Refinement of macromolecular structures by
774 the maximum-likelihood method. *Acta Crystallogr D Biol Crystallogr* **53**, 240-255 (1997).
775 28. C. J. Williams *et al.*, MolProbity: More and better reference data for improved all-atom
776 structure validation. *Protein Sci* **27**, 293-315 (2018).

777 29. A. Xiao *et al.*, CasOT: a genome-wide Cas9/gRNA off-target searching tool.
778 *Bioinformatics* **30**, 1180-1182 (2014).
779 30. A. Al-Arif, M. Blecher, Synthesis of fatty acyl CoA and other thiol esters using N-
780 hydroxysuccinimide esters of fatty acids. *J Lipid Res* **10**, 344-345 (1969).
781 31. T. J. Woodman *et al.*, Chiral inversion of 2-arylpropionyl-CoA esters by human alpha-
782 methylacyl-CoA racemase 1A (P504S)--a potential mechanism for the anti-cancer effects
783 of ibuprofen. *Chem Commun (Camb)* **47**, 7332-7334 (2011).
784 32. M. Pal, M. Khanal, R. Marko, S. Thirumalairajan, S. L. Bearne, Rational design and
785 synthesis of substrate-product analogue inhibitors of alpha-methylacyl-coenzyme A
786 racemase from Mycobacterium tuberculosis. *Chem Commun (Camb)* **52**, 2740-2743
787 (2016).
788 33. A. A. Cluntun *et al.*, The pyruvate-lactate axis modulates cardiac hypertrophy and heart
789 failure. *Cell Metab* **33**, 629-648 e610 (2021).
790 34. A. A. Cluntun *et al.*, The rate of glycolysis quantitatively mediates specific histone
791 acetylation sites. *Cancer Metab* **3**, 10 (2015).
792 35. M. J. Lukey *et al.*, Liver-Type Glutaminase GLS2 Is a Druggable Metabolic Node in
793 Luminal-Subtype Breast Cancer. *Cell Rep* **29**, 76-88 e77 (2019).
794 36. E. Sugarman *et al.*, Identification of Inhibitors of triacylglyceride accumulation in muscle
795 cells: comparing HTS results from 1536-well plate-based and high-content platforms. *J*
796 *Biomol Screen* **19**, 77-87 (2014).
797 37. M. Ghandi *et al.*, Next-generation characterization of the Cancer Cell Line Encyclopedia.
798 *Nature* **569**, 503-508 (2019).
799 38. H. Li *et al.*, The landscape of cancer cell line metabolism. *Nat Med* **25**, 850-860 (2019).
800